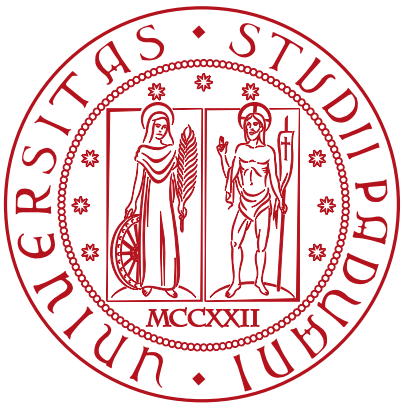

UNIVERSITÀ DEGLI STUDI DI PADOVA

Dipartimento di Fisica e Astronomia "Galileo Galilei"

Master Degree in Physics

Final Dissertation

Electro-optical lensing devices for RF sensing of cavity-laser mode-matching

Thesis supervisor

Prof./Dr. Giacomo Ciani

Thesis co-supervisor

Prof./Dr. Marco Bazzan

Candidate

Andrea Currò Dossi

Academic Year 2021/2022

"Chissà?
Forse nella notte me ne andrò...
scomparirò...
sotto le stelle."

U.C.D. April 4th 1947 (Trento)

Contents

Introduction

Both current (Virgo, LIGO, KAGRA) and future (eg. ET, Cosmic Explorer) interferometric gravitational-wave detectors are designed to be limited in most of their sensitivity band by quantum noise, which occurs at low frequencies in the form of quantum radiation pressure noise and at high frequencies as shot noise. To reduce this noise contributions the state-of-the-art of gravitational-wave interferometers makes use of nonclassical states of the electromagnetic field, called squeezed vacuum states, injecting them in the interferometer's dark port. To fully exploit this technique and overcome the so-called standard quantum limit, these squeezed states must be controlled by reflecting them off detuned optical resonators, called filter cavities, which allow to optimize the squeezing angle as a function of frequency. The ultimate reduction in quantum noise is however severely limited by light losses, for which one of the main contributions is represented by the imperfect matching between the mode of the squeezed and bright beams, and the various cavities present in the interferometer, including the filter cavities. To be able to monitor and actively correct this issue, an accurate, online mode-matching sensing technique is needed.

A sensing technique based on fast modulation of the Laguerre-Gauss 10 (LG10) mode is being developed by the ET-Virgo group in Laboratori Nazionali of Legnaro (INFN-LNL), in Padova, and it is based on an electro-optical lens (EOL), a device capable of changing its focal length at radio frequency. This generates sidebands whose beat signal with the carrier field reflected by the cavity contains information on the amount and type of mismatch.

The aim of this thesis is to characterize and study the performance of different EOL designs on a dedicated bench-top experiment. In particular two different approaches will be compared: one is the direct modulation of LG10 modes; the other is the modulation of the Hermite-Gauss 02 and 20 modes and their subsequent conversion in LG10 mode by an appropriate cylindrical telescope.

The following thesis work is divided into five chapters. Chapter 1 starts from a brief theoretical introduction on gravitational waves and then move on to the functioning of the interferometers and finally to the concept of noise and vacuum squeezing. The chapter 2 constitutes a theoretical background on laser beams and optical cavities. Chapter 3 goes into more detail of the main topic of the thesis: after a brief theoretical introduction on the concept of modematching and electro-optical modulation, it moves on to the description of the electro-optical lens prototypes to be characterized. Chapter 4 describes the experimental setup, the two tools used for the measurements and the theoretical expectations. Finally, in chapter 5, defines in more detail the two analysis methodologies used, in particular the wavefront variation sensing through a device called Shack-Hartmann and the modal analysis of the frequencies inside a triangular optical cavity using a photodiode. Finally, in this last chapter the experimental results obtained are presented.

Chapter 1

Gravitational waves

Historically, the study of the Universe relies almost exclusively on electromagnetic radiation (e.g. visible light, X-rays, radio waves and microwaves) and on subatomic particle (e.g. neutrinos) detection. The panorama of multimessanger physics has expanded enormously with the observation of gravitational wave signals. Since gravitational waves interact very weakly with matter, unlike EM radiation, the detection of this phenomenon give us the opportunity to look further back in time (close to the Big Bang) and to see the all the sky around us at the same time, due to the fact that the Earth does not stop the gravitational signal. These waves bring us information on phenomena that do not emit EM radiation, such as the coalescence of black holes (or, more generally, the binaries of black holes), or phenomena which would be extremely difficult to observe with EM signals due to the distance and required resolution. For this reason the detection of gravitational waves constitutes a new window on the universe, making it possible to observe space-time regions of the universe and phenomena that are normally inaccessible. On the other hand the extremely weak interaction of gravitational phenomena with matter makes revealing their passage very difficult. Today's detection methods are basically based on the measurement of the strain on the distance between two free falling masses.

Albert Einstein predicted the existence of gravitational waves in 1916, after publishing his final formulation of the field equations of general relativity: in simple terms gravitiational waves are ripples in space-time caused by violent and energetic processes in the Universe, such as colliding black holes, merging neutron stars, exploding stars, and possibly even the birth of the Universe itself. He found that massive accelerating objects would disrupt space-time injecting waves of undulating space-time with quadrupolar emission. Mathematically these waves are the solutions of the linearized weak-field equations: transverse waves of spatial strain that travel at the speed of light, generated by time variations of the mass quadrupole moment of the source [1].

1.1 Theory

General relativity provides a unified description of gravity as a geometric property of space and time. In particular, in the presence of non-null energy and momentum, the non-intertiality of reference systems results in a curvature in space-time. General relativity follows from Einstein's principle of equivalence: on a local scale it is impossible to distinguish between physical effects due to gravity and those due to acceleration. The relation is specified by the Einstein field equations: a system of second order partial differential equations, which describe the relation between the geometry of a four-dimensional pseudo-Riemannian manifold $g_{\mu\nu}$ representing spacetime, and the energy–momentum tensor $T_{\mu\nu}$ contained in that spacetime

$$R_{\mu\nu} - \frac{1}{2} g_{\mu\nu} R = \frac{8\pi G}{c^4} T_{\mu\nu} \tag{1.1}$$

with G the gravitational constant, c the speed of light, $R_{\mu\nu}$ and R respectivily the Ricci tensor and scalar. To understand where GWs come from, let's expand the Einstein equations around the flat-

space assuming that the induced space-time curvature is a small perturbation of the flat Minkowsky metric tesor $\eta_{\mu\nu}$

$$g_{\mu\nu} \simeq \eta_{\mu\nu} + h_{\mu\nu} \qquad |h_{\mu\nu}| \ll 1. \tag{1.2}$$

Now, expanding the equations of motion to linear order in $h_{\mu\nu}$, condition for the linearized theory, and using the gauge freedom to choose the De Donder gauge, is possible to rewrite the field equation as a simple wave equation

$$\Box h_{\mu\nu} = -\frac{16\pi G}{c^4} T_{\mu\nu} \tag{1.3}$$

with $\Box$ the flat space d'Alembertian

$$\Box = \eta_{\mu\nu}\partial^\mu\partial^\nu = -\left(\frac{1}{c^2}\right)\partial_t^2 + \nabla^2 \tag{1.4}$$

which implies that the GWs travel at the speed of light.

1.1.1 Interaction of GWs with test masses

To study the propagation of them, we are interested in the equation outside the source, i.e. where $T_{\mu\nu} = 0$,

$$\left(\frac{1}{c^2}\frac{\partial^2}{\partial t^2} + \frac{\partial^2}{\partial x_i^2}\right) h_{\mu\nu} = 0 \qquad i = 1, 2, 3. \tag{1.5}$$

At this point, imposing the transverse-traceless gauge, or TT gauge

$$h^{0\mu} = 0 \qquad h_i^i = 0 \qquad \partial^j h_{ij} = 0 \tag{1.6}$$

Eq. 1.5 has plane wave solutions

$$h_{\mu\nu}^{TT}(x) = A_{\mu\nu}(k^\mu) e^{jk_\rho x^\rho} \tag{1.7}$$

with $k^\mu = (\omega/c, \vec{k})$ the four-momentum or momentum energy and $A_{\mu\nu}$ the polarization tensor. Choosing z as the direction of propagation $\hat{n} = \vec{k}/|\vec{k}|$ of the wave vector

$$h_{xy}^{TT}(t, z) = \begin{pmatrix} h_+ & h_\times \\ h_\times & -h_+ \end{pmatrix}_{xy} \cos\left[\omega\left(t - \frac{z}{c}\right)\right] \tag{1.8}$$

with $h_{+,\times}$ the amplitudes of the plus and cross polarization of the wave. Fig. 1.1 schematically represents the effect produced by a gravitational wave in the two polarizations.

The amplitude of the GWs is given by the Einstein's quadrupole formula

$$h_{ij}^{TT}(t, r) = \frac{1}{r}\frac{2G}{c^4}\ddot{Q}_{ij}^{TT}\left(t - \frac{r}{c}\right) \tag{1.9}$$

where $\ddot{Q}_{ij}^{TT}$ is the second derivative of the quadrupole moment in the TT gauge. Typically the GW amplitude reaching Earth is of the order $h_0 \sim 10^{-21}$.

In the condition of Eq. 1.8, the space-time interval becomes

$$\begin{aligned} ds^2 = &-c^2dt^2 + dz^2 + \\ &+ \left(1 + h_+ \cos\left[\omega\left(t - \frac{z}{c}\right)\right]\right) dx^2 + \left(1 - h_\times \cos\left[\omega\left(t - \frac{z}{c}\right)\right]\right) dy^2 + 2h_\times \cos\left[\omega\left(t - \frac{z}{c}\right)\right] dxdy. \end{aligned} \tag{1.10}$$

Therefore the physical effect of a GW on two events or test masses, at $(t, x_1, 0, 0)$ and at $(t, x_2, 0, 0)$, is to change periodically their proper distance

$$s = (x_1 - x_2)[1 + h_+ \cos[\omega t]]^{1/2} \simeq L\left(1 + \frac{1}{2}h_+ \cos[\omega t]\right). \tag{1.11}$$

If these two test masses are mirrors between which a light beam travels back and forth, it is the proper distance that determines the time taken by the light to make a round trip, so the effect of the GW's passage can be detected measuring the round-trip time. This is the working principle of interferometers [14].

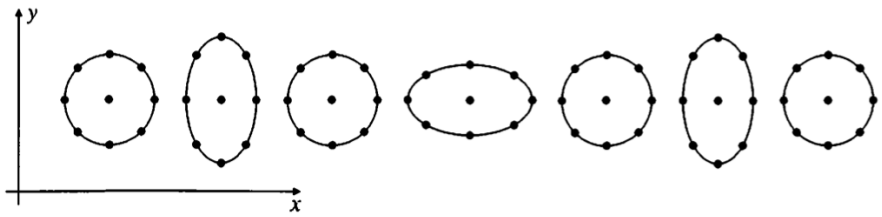

(a)

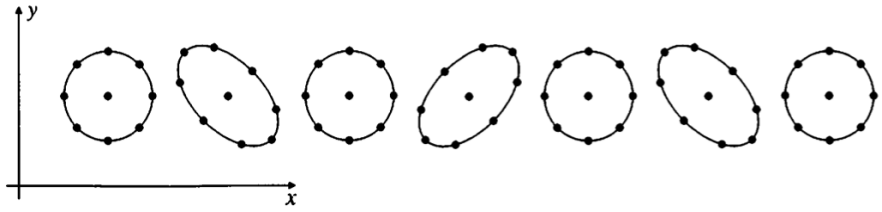

(b)

Figure 1.1: The effect on a circle of test particlesr of a gravitational wave traveling perpendicular to the xy plane in the two polarizations. (a) Plus polarization h_+ (b) Cross polarization $h_\times$ [7].

1.2 Virgo

A GW interferometer is an extremely complex instrument whose degrees of freedom must be kept under control with extraordinary accuracy. All modern interferometers are based on the Michelson scheme: it consists of a monochromatic light source, a laser, whose light is sent on a beam-splitter which separates the light into two beams, with equal probability amplitudes, traveling in two orthogonal arms. At the end of each arm a mirror reflects the laser beam back to the beam-splitter to generate an interference pattern which is read by a photodetector. Any length variation between the two arms results in a variation of the power at the photodetector. Because of the quadrupolar nature of the gravitational wave, the plus polarization, which for example propagates in the $-\hat{z}$ direction, will cause a variation on the arm length of $\pm\delta L$ in the $\hat{y}$ direction. At the same time the other arm will change by $\mp\delta L$ in the $\hat{x}$ direction. The differential arm motion will produce a phase change in the recombined beam of

$$\delta\phi = \frac{4\pi}{\lambda}\delta L. \tag{1.12}$$

It is possible to find out that the optimal length of the arms is

$$L \simeq 750\, km \left(\frac{100\, Hz}{f_{GW}}\right). \tag{1.13}$$

Arms of hundreds of kms are impossible to obtain in a ground-based interferometer, for practical and financial reasons. The idea is to fold the optical path of light, making it bounce back and forth many times in each arm. The number that quantifies the bounces of the laser in the arms is defined by the Finesse (see Eq. 2.25) and is approximately $\mathcal{F} \sim 400$. The solution is to trasform each arm into a Fabry-Pérot cavity (see Sec. 2.3). With this expedient the phase change is enhanced

$$\delta\phi_{FP} = \frac{8\mathcal{F}}{\lambda}\delta L. \tag{1.14}$$

Another important improvement of a GW interferometer, is to use a resonant cavity (see Sec. 2.3) as power recycling cavities.

Fig. 1.2 shows the basic layout of the Advanced Virgo interferometer. A suspended, triangular Fabry-Pérot cavity serves as an input mode cleaner to clean up the spatial profile of the laser beam, suppress input beam jitter, clean polarization, and to help stabilize the laser frequency. The Michelson

interferometer is enhanced by two 4 km long resonant arm cavities, which increase the optical power in the arms by a factor of $\simeq 270$. A power recycling mirror and a signal recycling mirror are used respectively to increase the circulating power in the interferometer and to broaden the response of the detector beyond the linewidth of the arm cavities. Eventually an output mode cleaner rejects the unwanted spatial and frequency components of the light, before the signal is detected by the main photodetectors [14]. In total there are six cavities inside an interferometer.

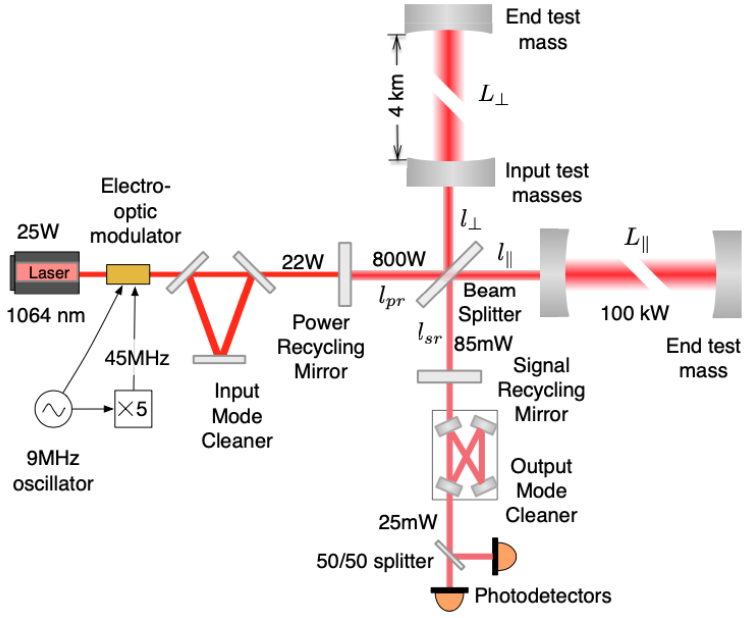

Figure 1.2: Layout of an Advanced LIGO detector [15].

1.3 Noise

The sensitivity at which a GW interferometer must aim is extremely ambitious. As a benchmark, as we already anticipated in Sec. 1.1.1, a typical GW amplitude, which releases an energy of $\sim M_\odot$ (i.e. solar masses), is of the order of $h \sim 10^{-21}$. The corrisponding displacement of the mirror of an interferometer is $\delta L \sim 10^{-18}\ m$, which means that we aim at measuring a phase shift $\delta\phi_{FP} \sim 10^{-8}\ rad$. Since these values are extremely small, to detec a signal, it is important to minimize all the possible sources of noises. They can be divided in technical noises, due to the enviroment or to the interferometer design (e.g. seismic and Newtonian noise, thermal noise, fluctiation of the laser power and frequecy, scattered light inside the arms, vacuum control) and fundamental noises, related to the fundamental physics and to the detection procedure. In particular, currente generation GW detectors are designed to be limited by quantum noise in most of their sensitivity band (see Sec. 1.3.1) [14].

The standard quantum limit of an interferometer refers to the quantum nature of light and it is a combined effect of two mechanism, both due to the poissonian distribution of photons in a light beam: photon-counting error shot noise and fluctuations in radiation pressure on the masses quantum radiation-pressure [8].

- Shot noise: it is the high-frequency intensity noise of a laser. This originates from the Possonian distribution on the number of photons that arrive on the photodetector. It is possible to obtain the strain sensitivity due to this effect

$$S_n^{1/2}(f)\Big|_{shot} = \frac{\lambda_0}{4\pi L}\sqrt{\frac{2\hbar\omega_0}{P_0}} \sim \frac{1}{\sqrt{P_0}} \tag{1.15}$$

  where ω_0 and P_0 are respectively the frequency and power of the laser and L is the arm length.

- Radiation pressure: it is the low-frequency intensity noise of a laser. Since the number of photons arriving on each mirror fluctuates, the pressure contribution, due to the impact of photons that release momentum, fluctuats too, generating a stochastic force that shakes the mirrors. The strain sensitivity of this mechanism is

$$S_n^{1/2}(f)\Big|_{rad} = \frac{4}{ML(2\pi f)^2}\sqrt{\frac{2\hbar\omega_0 P_0}{c^2}} \sim \sqrt{P_0} \tag{1.16}$$

  with f the GW frequency and M the mass of the mirror.

Now, consider the combined effect of these noise sources, and minimize with respect to P_0, is possible to find the minimum value of the spectal density also known as standard quantum limit [14]

$$S_{SQL}^{1/2}(f) = \frac{1}{2\pi f L}\sqrt{\frac{8\hbar}{M}}. \tag{1.17}$$

1.3.1 Vacuum squeezing and the problem of mode mismatch

A squeezed state of light is a nonclassical states which presents reduced uncertainty in one of the quadrature components of the EM field; due to the Heisenberg Uncertainty principle, the other quadrature must however show increased uncertainty. By injecting a squeezed vacuum state from the output port of the interferometer, one can thus decrease shot noise (linked to the so called phase quadrature) while increasing quantum radiation pressure noise (linked to the so called amplitude quadrature), or vice versa, depending on the "direction" in which the uncertainty ellipse is squeezed (squeezing angle). This technology has been used in the last observing run of both the Virgo and LIGO interferometers to reduce shot noise at high frequency, since radiation pressure at low frequency was anyway masked by other noises [9].
If one wants to gain an advantage simultaneously in the whole band of the interferometer, the squeezing angle must be varied as a function of frequency, so that at high frequency one would reduce shot noise and increase radiation pressure noise (which however is negligible), and the opposite at low frequency. The principle is illustrated in Fig. 1.3. This technique is being implemented in the current upgrades of the detectors by reflecting the squeezed light field off of a special detuned resonator called *filter cavity*, so that it gains a phase rotation dependent on its frequency offset form the carrier.

Unfortunately squeezed light is severely limited by optical losses in the detector, which destroy the crucial feature of the technique, i.e. the reduced noise in one of the two quadrature phases, or, in other words, the coherency condition. To minimize the losses due to the imperfect agreement, or mismatch (Sec. 2.4), between the laser beam and the optical cavity where it circulates, one has to provide an active correction system that keep the setup aligned.

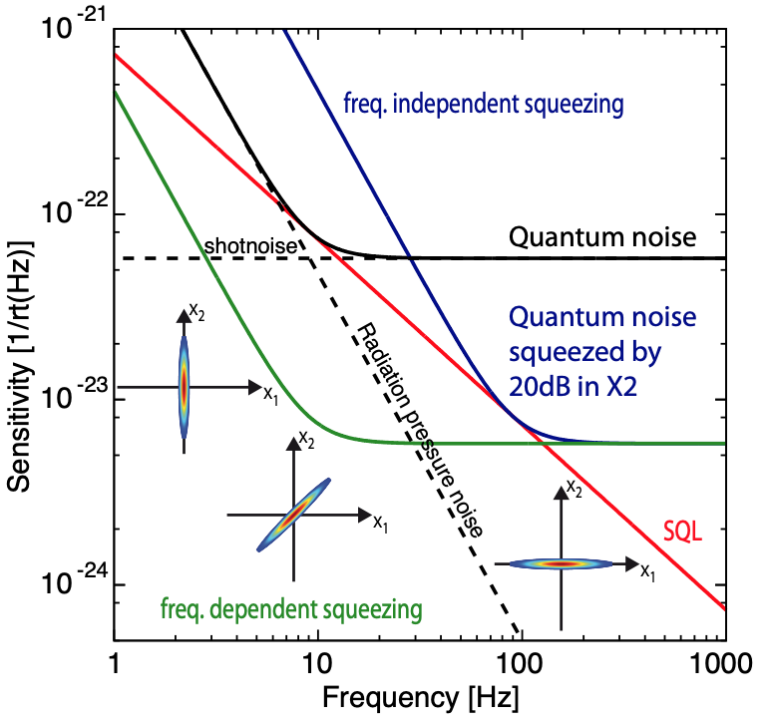

Figure 1.3: Beating the standard quantum limit in position meter with frequency-dependent squeezed light [2].

Chapter 2

Theoretical background

2.1 Gaussian beams

In optics and in particulare in laser physics, laser beams are often described in terms of Gaussian beams, i.e. light beams where the electric field profile in a plane perpendicular to the beam axis can be described with a Gaussian function. This way of treating the light rays arises from a possible solution of the paraxial Helmholtz equation [18].

Starting from the complex amplitude of a monochromatic paraxial wave and imposing that the complex envelope must satisfy the paraxial Helmholtz equation, the simplest possible solution yields to the paraboloid wave

$$A(\vec{r}) = \frac{A_1}{q(z)} \exp\left[-jk\frac{\rho^2}{2q(z)}\right] \qquad \rho^2 = x^2 + y^2 \qquad A_1 = const \qquad x, y \ll z \tag{2.1}$$

with $\vec{r} = (x, y, z)$, laser beam propagation axis $\hat{z}$ and A_1 normalization constant which corresponds to the amplitude in $(0, 0, 0)$.
This Gaussian complex amplitude solution is obtained directly from a shifted version of the paraboloid wave equation by a purely imaginary term. This choice is done to obtain a real term in the exponential that produces a rapidly decay of the beam intensity away from the optical axis. This condition is necessary otherwise the approximations, both the paraxial one, and that of approximating a spherical surface with a paraboloid, fall. In particular, the z coordinate is replaced by the so-called Kogelnik or complex q-parameter

$$z \to q(z) = z + jz_R \tag{2.2}$$

with z_R known as the Rayleigh range. The real and imaginary part of this complex parameter can be separated defining two real functions of z

$$\frac{1}{q(z)} = \frac{1}{z + jz_R} = \frac{1}{R(z)} - j\frac{\lambda}{\pi W^2(z)} \tag{2.3}$$

with $R(z)$ the wavefront radius of curvature and $W(z)$ the beam width.
Eventually the complex ampilude becomes

$$U(\vec{r}) = A_0 \frac{W_0}{W(z)} \exp\left[-\frac{\rho^2}{W^2(z)}\right] \exp\left[-jkz - jk\frac{\rho^2}{2R(z)} + j\phi(z)\right] \tag{2.4}$$

and the beam parameters

$$W(z) = W_0\sqrt{1 + \left(\frac{z}{z_R}\right)^2} \qquad R(z) = z\left[1 + \left(\frac{z_R}{z}\right)^2\right] \qquad \phi(z) = \tan^{-1}\frac{z}{z_R} \qquad W_0 = \sqrt{\frac{\lambda z_R}{\pi}}. \tag{2.5}$$

The last phase term in 2.4 is the so called Gouy phase and corresponds the accumulated phase of this paraxial wavefront in relation to a plane wave.

2.1.1 Hermite-Gauss and Laguerre-Gauss

The complex amplitude found, or gaussian beam, is the lowest order solution of an infinite family of higher order solutions, which also satisfy the paraxial Helmholtz equation. The higher order solutions to the same equations can be expressed in terms of Hermite-Gauss (HG) functions in rectangular coordinates or of Laguerre-Gauss (LG) functions in cylindrical coordinates [19]. These higher order modes exhibit non-Gaussian intensity distributions but share the same wavefronts of the Gaussian beam. Such beams are able to match the curvatures of spherical mirrors of large radius, such as those that form an optical resonator, and reflect between them almost unaltered. Such self-reproducing waves are called the modes of the resonator. The HG and LG modes form a complete orthogonal basis, orthonormal if properly normalized. This means that any laser beam can be expressed as a linear combination of modes of different order which evolve with different phase and therefore, on different planes, the profile of a generic beam changes because of the interference between the modes in which it is decomposed [18].
The decomposition in the Hermite-Gauss base gives

$$U_{nm}(x,y,z) = \sqrt{\frac{2}{\pi W^2(z) 2^{n+m} m! n!}} H_l\left[\frac{\sqrt{2}x}{W(z)}\right] H_m\left[\frac{\sqrt{2}y}{W(z)}\right] \exp\left[-\frac{x^2+y^2}{W^2(z)}\right] \exp\left[-\frac{k(x^2+y^2)}{2R(z)}\right] \exp[-jkz] \exp\left[j((n+m)+1)\arctan\frac{z}{z_R}\right] \tag{2.6}$$

and in the Laguerre-Gauss base

$$U_{pl}(r,\psi,z) = \sqrt{\frac{2p!}{\pi(|l|+p)!}} \frac{1}{W(z)} \left(\frac{\sqrt{2}r}{W(z)}\right)^{|l|} L_p^{|l|}\left[\frac{2r^2}{W^2(z)}\right] \exp\left[-\frac{r^2}{W^2(z)}\right] \exp\left[-\frac{kr^2}{2R(z)}\right] \exp[-jkz] \exp[+jl\psi] \exp\left[j((|m|+2p)+1)\arctan\frac{z}{z_R}\right] \tag{2.7}$$

Tab. 2.1 and 2.2 list the first elements of the respective bases; in order to simplify the notation the higher order modes are described as a function of the fundamental mode.

nm	$N+1$	H_nH_m	$U_{nm}(x,y,z)$
00	1	1	$\sqrt{\frac{2}{\pi}}\frac{1}{W(z)} \exp\left[-\frac{x^2+y^2}{W^2(z)} - \frac{k(x^2+y^2)}{2R(z)} - jkz + j\arctan\frac{z}{z_R}\right]$
10	2	$2\frac{\sqrt{2}x}{W(z)}$	$2\frac{x}{W(z)} \exp\left[j\arctan\frac{z}{z_R}\right] U_{00}(x,y,z)$
01	2	$2\frac{\sqrt{2}y}{W(z)}$	$2\frac{y}{W(z)} \exp\left[j\arctan\frac{z}{z_R}\right] U_{00}(x,y,z)$
11	3	$8\frac{xy}{W^2(z)}$	$4\frac{xy}{W(z)} \exp\left[2j\arctan\frac{z}{z_R}\right] U_{00}(x,y,z)$
20	3	$2\left(4\frac{x^2}{W^2(z)} - 1\right)$	$\frac{1}{\sqrt{2}}\left(4\frac{x^2}{W^2(z)} - 1\right) \exp\left[2j\arctan\frac{z}{z_R}\right] U_{00}(x,y,z)$
02	3	$2\left(4\frac{y^2}{W^2(z)} - 1\right)$	$\frac{1}{\sqrt{2}}\left(4\frac{y^2}{W^2(z)} - 1\right) \exp\left[2j\arctan\frac{z}{z_R}\right] U_{00}(x,y,z)$

Table 2.1: List of Hermite-Gauss modes, polynomials and total complex amplitude. The order number here is defined as $N = n + m$.

2.2 Ray matrix

When light waves propagate through and around objects whose dimensions are much greater than the wavelength of the light ($\lambda \ll 1$), the behavior of light can be adequately described by rays obeying a set of geometrical rules. This model of light is called ray optics.

Paraxial rays travel at small inclinations with respect to the optical axis and the change in the position and inclination of a paraxial ray as it travels can be effeciently described by the use of a matrix. Matrix

pl	$N+1$	$L_p^{\lvert l\rvert}$	$U_{pl}(r,\psi,z)$
00	1	1	$\sqrt{\frac{2}{\pi}}\frac{1}{W(z)}\exp\left[-\frac{r^2}{W^2(z)}-j\frac{z_R r^2 z}{W_0^2(z^2+z_R^2)}+j\arctan\frac{z}{z_R}\right]$
10	3	$\left(1-\frac{2r^2}{W^2(z)}\right)$	$\left(1-\frac{2r^2}{W^2(z)}\right)\exp\left[2j\arctan\frac{z}{z_R}\right]U_{00}(r,\psi,z)$
01	2	1	$\frac{\sqrt{2}r}{W(z)}\exp\left[-j\psi+j\arctan\frac{z}{z_R}\right]U_{00}(r,\psi,z)$
11	4	$\left(2-\frac{2r^2}{W^2(z)}\right)$	$\frac{\sqrt{2}r}{W(z)}\left(2-\frac{2r^2}{W^2(z)}\right)\exp\left[-j\psi+3j\arctan\frac{z}{z_R}\right]U_{00}(r,\psi,z)$
20	5	$\left(1-\frac{4r^2}{W^2(z)}+\frac{2r^4}{W^4(z)}\right)$	$\left(1-\frac{4r^2}{W^2(z)}+\frac{2r^4}{W^4(z)}\right)\exp\left[4j\arctan\frac{z}{z_R}\right]U_{00}(r,\psi,z)$
02	3	1	$\frac{\sqrt{2}r^2}{W^2(z)}\exp\left[-2j\psi+2j\arctan\frac{z}{z_R}\right]U_{00}(r,\psi,z)$

Table 2.2: List of Laguerre-Gauss modes, polynomials and total complex amplitude. The order number here is defined as $N=|l|+2p$.

optics is an algebric tool for tracing paraxial rays that travel through an optical system, i.e. a set of optical components placed between two transverse planes at different axial distances z_1 and z_2, referred to as the input and output planes. The system is characterized completely by its effect on an incoming ray of arbitrary crossing point. The system steers the ray so that it emerges from the output plane with a new position and direction (y_2,θ_2).

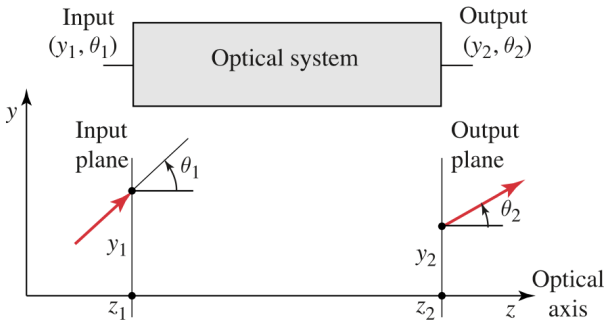

Figure 2.1: The position and direction of a paraxial ray is modified by an optical system [18].

In the paraxial approximation, when all angles are sufficiently small, the relation between $(y_{1,2},\theta_{1,2})$ is linear and can generally be written in matrix form, also known as ray-transfer matrix, as

$$\begin{pmatrix} y_2 \\ \theta_2 \end{pmatrix} = \begin{pmatrix} A & B \\ C & D \end{pmatrix} \begin{pmatrix} y_1 \\ \theta_1 \end{pmatrix}. \tag{2.8}$$

The convenience of using matrix methods lies in the fact that the ray-transfer matrix of a cascade of optical components is a product of the ray-transfer matrix of the individual components. Matrix optics therefore provides a formal mechanism for describing complex optical systems in the paraxial approximation [12].
Tab. 2.3 contains some example of ray-transfer matrix for common optical systems.

It can be shown that this formalism can be also applied to gaussian beams, using the same ray-trasferm matrix of conventional ray optics. Since the parameter which completely characterizes a Gaussian beam is the q-parameter, for an arbitrary paraxial optical system, the transmitted beam is described by Collins' rule

$$q_2 = \frac{Aq_1+B}{Cq_1+D}. \tag{2.9}$$

2.2.1 Imaging

By definition two image (or conjugate) planes describe an optical system where the characteristics of a beam are imaged from an input to an output plane. For a telescope this means that the beam

Optical system	Ray transfer matrix
Propagation in a medium	$\begin{pmatrix} 1 & \frac{d}{n} \\ 0 & 1 \end{pmatrix}$
Refraction at a planar boundary	$\begin{pmatrix} 1 & 0 \\ 0 & \frac{n_1}{n_2} \end{pmatrix}$
Refraction at a spherical boundary	$\begin{pmatrix} 1 & 0 \\ -\frac{(n_2-n_1)}{n_2 R} & \frac{n_1}{n_2} \end{pmatrix}$
Transmission through a thin lens	$\begin{pmatrix} 1 & 0 \\ -\frac{1}{f} & 1 \end{pmatrix}$
Reflection from a planar mirror	$\begin{pmatrix} 1 & 0 \\ 0 & 1 \end{pmatrix}$

Table 2.3: Example of some ray transfer matrix for different optical systems.

profile at the aperture plane or midplane of one amplifier can be imaged as an essentially identical but magnified beam profile at the midplane or image plane of the next amplifier. Moreover Fermat's principle says that *all rays connecting two conjugate points must have the same optical path length between these two points* which for a gaussian beam means that in the two planes the Gouy phase coincide [19].
In the case of a two lens optical system, let's define $f_{1,2}$ the focal lengths of the two lenses and $d_{1,2,3}$ the distances respectively between the input plane and the first lens, between the two lenses and between the second lens and the output plane. Using the ray transfer matrix analysis the resulting matrix for the total optical setup becomes

$$\begin{pmatrix} y_2 \\ \theta_2 \end{pmatrix} = \begin{pmatrix} 1 & d_3 \\ 0 & 1 \end{pmatrix} \begin{pmatrix} 1 & 0 \\ -\frac{1}{f_2} & 1 \end{pmatrix} \begin{pmatrix} 1 & d_2 \\ 0 & 1 \end{pmatrix} \begin{pmatrix} 1 & 0 \\ -\frac{1}{f_1} & 1 \end{pmatrix} \begin{pmatrix} 1 & d_1 \\ 0 & 1 \end{pmatrix} \begin{pmatrix} y_1 \\ \theta_1 \end{pmatrix}. \tag{2.10}$$

When this system is setup for imaging, y_2 is independent of θ_1 (i.e. $B = 0$). In this case one obtains a condition on d_3

$$d_3 = \left[\frac{1}{f_2} - \frac{1}{d_2} \frac{\left(\frac{1}{d_1} - \frac{1}{f_1}\right)}{\left(\frac{1}{d_1} + \frac{1}{d_2} + \frac{1}{f_1}\right)} \right]^{-1}. \tag{2.11}$$

It is easy to see that if $B = 0$, the magnification factor is simply given by A [5]

$$M = 1 - \frac{d_2}{f_1} + \frac{\left(\frac{1}{d_1} + \frac{1}{d_2} - \frac{1}{f_1}\right)\left(\frac{d_2}{f_1 f_2} - \frac{1}{f_1} - \frac{1}{f_2}\right)}{\frac{1}{f_2}\left(\frac{1}{d_1} + \frac{1}{d_2} - \frac{1}{f_1}\right) - \frac{1}{d_2}\left(\frac{1}{d_1} - \frac{1}{f_1}\right)}. \tag{2.12}$$

2.3 Optical resonators

An optical resonator (or resonant optical cavity) is an arrangement of optical components, such as mirrors, crystals or optical fibers, which allows a beam of light to circulate in a closed path producing a travelling wave at certain frequencies. Optical cavities are extensively used to enhance the sensitivity of gravitational wave detectors and others high precision optical experiments.
The simplest kind of optical resonator consists of just two perfect plane mirrors set up facing each other, called Fabry-Pérot cavity (Fig. 2.2(a)). These mirrors can in practice trap the beam that will bounce back and forth between the two mirrors. This set of trapped Hermite-gaussian modes form, to a first approximation, a set of resonant modes for the cavity [19].

To describe a Fabry-Pérot cavity let's suppose that a steady-state sinusoidal optical signal $\tilde{E}_i \in \mathbb{C}$ is incident on one of the cavity mirrors. The circulating signal amplitude inside the cavity is

$$\tilde{E}_c = jt_1\tilde{E}_i + \tilde{g}_{rt}(\omega)\tilde{E}_c \rightarrow \tilde{E}_c = \frac{jt_1}{1 - \tilde{g}_{rt}(\omega)}\tilde{E}_i \tag{2.13}$$

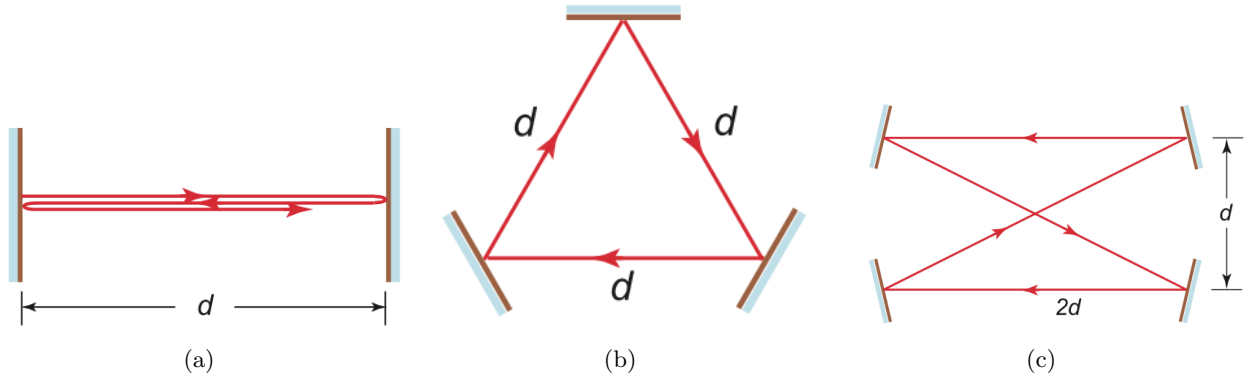

Figure 2.2: Traveling-wave resonator. (a) Two-mirror planar or Fabry-Pérot resonator (b) Three-mirror ring resonator. (c) Four-mirror bow-tie resonator [18].

with t_1 the first mirror amplitude transmittivity and $\tilde{g}_{rt}(\omega)$ the net complex round trip gain for a wave making one complete transit around the interior of the resonant cavity

$$\tilde{g}_{rt}(\omega) = r_1 r_2 (r_3 ...) \exp\left[-\alpha_0 p - \frac{j\omega p}{c}\right], \tag{2.14}$$

with $|r_{1,2,3}| < 1$ the wave-amplitude reflection coefficients of the mirrors, p the perimeter or the round-trip path length, α_0 the voltage absorption coefficient (or other possible kinds of internal losses and gains) of the material inside the cavity and the last factor of the exponential, considering here plane waves with frequency ω, is a phase shift or propagation factor associated with the round trip. Considering an ideal cavity whose internal losses are negligible, i.e. $\alpha_0 \ll 1$. If

$$\frac{j\omega p}{c} = 2\pi n \quad \text{with} \quad n \in \mathbb{Z} \tag{2.15}$$

then

$$\frac{\tilde{E}_c}{\tilde{E}_i} = \frac{j t_1}{1 - r_1 r_2 (r_3 ...)}. \tag{2.16}$$

If the reflection coefficients $r_{1,2,3} \sim 1$ the above ratio is very large. This is the resonance frequency condition for the laser cavity

$$\omega_n = 2\pi n \frac{c}{p} \tag{2.17}$$

which are also called cavity axial modes. Resonant frequencies form an evenly spaced combination and the distance (in frequency)

$$\Delta\omega_{FSR} = c/p \tag{2.18}$$

is called free spectral range or axial-mode interval between consecutive resonant transverse modes. Physically this means that when the traveling wave is at frequency ω_n it is trapped and interferes constructively with itself, so the field inside the cavity raises to a very large value. Therefore the circulating intensity inside the cavity at these resonances becomes many times larger than the incident one. In general the circulating intensity is simply given by the square modulus of the circulating electric field

$$\left.\frac{I_c}{I_i}\right|_{\omega=\omega_n} = \frac{t_1^2}{\left[1 - r_1 r_2 (r_3 ...) e^{-\alpha_0 p}\right]^2}. \tag{2.19}$$

Is possible to obtain a relation also for the transmitted and reflected field, being careful to consider if the round-trip travelled by the beam inside the cavity is completed or not, in the Fabry-Pérot case

$$\tilde{E}_t = j t_2 \exp\left[-\frac{\alpha_0 p}{2} - \frac{j\omega p}{2c}\right] \tilde{E}_c = -\frac{t_1 t_2 \exp\left[-\frac{\alpha_0 p}{2} - \frac{j\omega p}{2c}\right]}{1 - r_1 r_2 \exp\left[-\alpha_0 p - \frac{j\omega p}{c}\right]} \tilde{E}_i \tag{2.20}$$

$$\tilde{E}_r = r_1\tilde{E}_i + jt_1r_2\exp\left[-\alpha_0 p - \frac{j\omega p}{c}\right]\tilde{E}_c = \frac{r_1 - t_1^2 r_2\exp\left[-\alpha_0 p - \frac{j\omega p}{c}\right]}{1 - r_1 r_2\exp\left[-\alpha_0 p - \frac{j\omega p}{c}\right]}\tilde{E}_i. \tag{2.21}$$

A special situation arises when the input mirror power reflectivity $R_1 = 1 - T_1 = 1 - t_1^2$ is exactly equal to the additional loss term given by $R_2\exp[-2\alpha_0 p]$. In this case the two terms in the reflection expression cancel out, and the net reflection coefficient becomes exactly zero at resonance. This is often called the impedance-matched situation.

Using 2.19, the transmitted intensity if $\alpha_0 \ll 1$ becomes

$$I_t = I_c T = \frac{t_2^2 t_1^2}{\left|1 - \tilde{g}_{rt}(\omega)\right|^2}. \tag{2.22}$$

The linewidth of the cavity resonance is defined as its Full Width at Half Maximum (FWHM), referred to the power curve (either circulating or transmitted)

$$\frac{1}{2} = \frac{I_t(\omega_{HM})}{I_t(\omega_n)} = \frac{\left|1 - \tilde{g}_{rt}(\omega_n)\right|^2}{\left|1 - \tilde{g}_{rt}(\omega_{HM})\right|^2} \tag{2.23}$$

which gives

$$\Delta\omega_{HM} = \frac{4c}{p}\arcsin\left[\frac{1 - \tilde{g}_{rt}}{2\sqrt{\tilde{g}_{rt}}}\right] \simeq \Delta\omega_{FSR}\frac{1 - \tilde{g}_{rt}}{2\sqrt{\tilde{g}_{rt}}}. \tag{2.24}$$

The ratio of the FSR to the FWHM is called Finesse [14] [3]

$$\mathcal{F} = \frac{\Delta\omega_{FSR}}{\Delta\omega_{HM}} = \frac{\pi\sqrt{\tilde{g}_{rt}}}{1 - \tilde{g}_{rt}} \tag{2.25}$$

It is immediate to see that this parameter is a measure of how narrow the resonances are in relation to their frequency distance: a high finesse means sharp resonances. Moreover it is fully determined by the resonator losses and is independent of the resonator length.

2.3.1 Stable spherical-mirror resonator

Up to now there has been talk of ideal optical resonators that trap plane waves thanks to the use of plane mirrors of infinite dimensions. However, this scenario is not possible. A real optical resonator consists of spherical mirrors that trap Gaussian beams (see Sec. 2.1.1). To be supported by a cavity, in a real Fabry-Pérot cavity, the radii of curvature of the wavefronts of the Gaussian beam have to match the radii of the spherical mirrors, which are separated by a distance d.

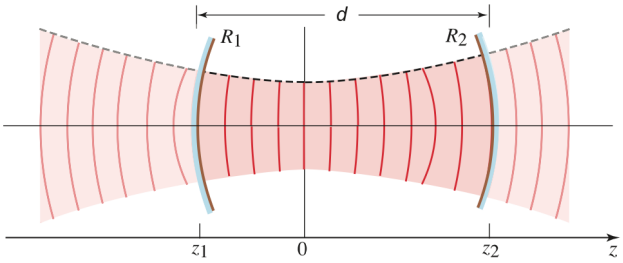

Figure 2.3: Fitting a Gaussian beam inside a spherical mirror resonator [18].

The z axis is defined by the centers of curvature of the mirrors (Fig. 2.3). Calling $z_{1,2}$ the mirrors' positions, to determine a suitable value for the beam Rayleigh range is necessary to impose the following conditions

$$\begin{cases} z_2 = z_1 + d \\ R_1 = z_1 + \dfrac{z_R^2}{z_1} \\ -R_2 = z_2 + \dfrac{z_R^2}{z_2}. \end{cases} \tag{2.26}$$

Solving the system it results

$$\begin{cases} z_1 = \dfrac{-d(R_2 + d)}{R_2 + R_1 + 2d} \\ z_2 = \dfrac{d(R_1 + d)}{R_2 + R_1 + 2d} \\ z_R^2 = \dfrac{-d(R_1 + d)(R_2 + d)(R_1 + R_2 + d)}{(R_2 + R_1 - 2d)^2}. \end{cases} \tag{2.27}$$

To find real solutions fot the above system, $z_R \in \mathbb{R}$. An imaginary value of Rayleigh range would signify an unconfined solution of the Helmholtz equation because otherwise the condition introduced at the beginning of the Sec. 2.1 falls, i.e. having a rapid decay of the beam intensity away from the optical axis. The condition $z_R^2 > 0$ is equivalent to

$$\begin{gathered} 0 \leq \left(1 + \frac{d}{R_1}\right)\left(1 + \frac{d}{R_2}\right) \leq 1 \\ 0 \leq g_1 g_2 \leq 1 \end{gathered} \tag{2.28}$$

which is known as the confinement condition written in terms of the cavity g-parameter. Fig. 2.4 shows the so-called stability diagram and some remarkable configurations of stable resonators.

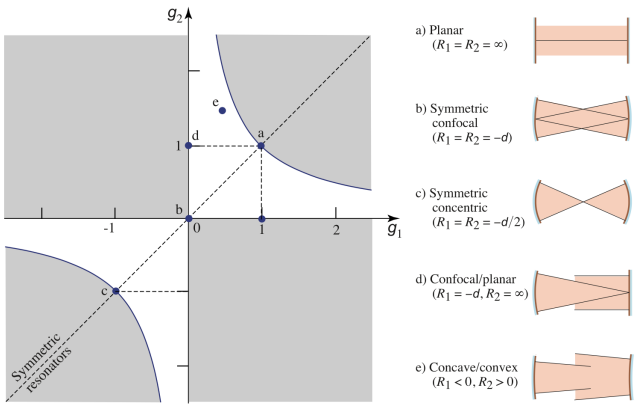

Figure 2.4: Resonator stability diagram [18].

Higher-order modes

In the Sec. 2.1.1 we have seen that the Gaussian beam is not the only solution for the Helmholtz paraxial equation. The HG (or LG) mode family of order (n, m) is itself a solution. So all members of the HG family of beams represent modes of the spherical-mirror resonator. However the resonance frequencies of higher order modes depend on the indices because of the dependence of the Gouy phase shift on n and m. In general after a round-trip inside the cavity, each mode fulfills this equation

$$2kd - 2(n + m + 1)(\phi(z_2) - \phi(z_1)) = 2\pi q \qquad q \in \mathbb{Z} \tag{2.29}$$

where the index q defines the so called longitudinal or axis modes which are separated by one free spectral range. Now using the fact that the wavenumber is defined as $k = \omega_{q,n,m}/c$ and that the Gouy phase can be written as $\phi = 2\pi\omega/\Delta\omega_{FSR}$ one obtains

$$\omega_{q,n,m} = (q + (n + m + 1)(\pm\sqrt{g_1 g_2}))\omega_{FSR}. \tag{2.30}$$

The direct consequence of this equation is that the higher order modes with the same order number (see Tab.2.1) resonate at the same frequency. The confinement condition (Eq. 2.28) is important in the latter case because it sets the higher order modes' frequency spacing inside the free spectral range [11].

2.4 Mode-matching

For a beam to properly resonate inside a stable optical cavity it must satisfy the following two conditions: the laser frequency is at the cavity resonance frequency and the laser beam wavefront matches the curvature of the cavity reflection mirrors. The mode mismatch consists in the failure in meeting the second condition, the geometric one [20].
A mathematical way to see the mismatch between a Gaussian beam and a cavity is to use the q-parameter, defined in Eq. 2.3. We then consider a cavity whose waist is in z_c and whose resonant modes are described by the parameter $q_c(z)$ and a Gaussian beam in the fundamental mode that enters the cavity with a parameter $q_i(z)$. When:

$$q_c(z_c) \neq q_i(z_c) \tag{2.31}$$

there is a mismatch between beam and cavity. The coupling of a mode refers to how good a spatial mode in a base is represented in another base: to quantify the decoupling between the cavity and the incoming beam it is therefore necessary to project the beam into the base of the cavity and calculate the coupling coefficients to the higher order modes through an overlapping integral. The procedure that allows to reduce this decoupling as much as possible is called mode-matching.

2.4.1 Mismatch description with LG modes

To mathematically describe the mismatch between cavity and laser beam let's introduce two families of LG modes, one defined by the q-parameter q_i of the input beam, V_{ij}, and one by the fundamental mode supported by the cavity U_{kl}, q_c. If the laser is perfectly aligned with the resonator

$$\int U_{ij} V^*_{lm} dxdy = \delta_{il}\delta_{jm}. \tag{2.32}$$

If instead there is a mismatch, the matrix for the base change is not diagonal anymore. Consider the mismatch only given by differences in the waist size δw_0 and position δz_0 and expand these LG modes in their McLaurin series up to the second order, around $(\delta w_0, \delta z_0) = (0, 0)$. The goal is to write the beam modes in the cavity basis.
Let's treat first the case of a laser beam with a non-null mismatch given only by waist size differences parametrize by $\beta = \delta w_0/w_0$. Using the McLaurin series expansion

$$\begin{aligned} V_{00}(r, w_0 + \delta w_0) &\simeq V_{00}(r, w_0) + \delta w_0 \frac{\partial V_{00}}{\partial w_0}(r, z)\bigg|_{z=0} + \frac{\partial w_0^2}{2}\frac{\partial^2 V_{00}}{\partial w_0^2}(r, z)\bigg|_{z=0} \\ &= \left(1 - \frac{\beta^2}{2}\right) V_{00}(r, w_0) + \left(-\beta + \frac{\beta^2}{2}\right) V_{10}(r, w_0) + \beta^2 V_{20}(r, w_0) \end{aligned} \tag{2.33}$$

written as a linear composition of LG modes. In the same way

$$V_{10}(r, w_0 + \delta w_0) \simeq \beta V_{00}(r, w_0) + V_{10}(r, w_0) - 2\beta V_{20}(r, w_0). \tag{2.34}$$

Consider now the case where there is a mismatch between the waist positions, it is parametrized by $\gamma = \delta z_0/2z_R$. Also in this case is possible to expand in a linear combination of LG modes, with $z_0 = 0$ for convenience. One obtain

$$\begin{aligned} V_{00}(r, \delta z_0) &\simeq V_{00}(r, w_0) + \delta z_0 \frac{\partial V_{00}}{\partial z}(r, z)\bigg|_{z=0} + \frac{\partial z_0^2}{2}\frac{\partial^2 V_{00}}{\partial z^2}(r, z)\bigg|_{z=0} \\ &= V_{00}(r, w_0)\left(1 + j\gamma - \gamma^2\right) + V_{10}(r, w_0)\left(j\gamma - 2\gamma\right) - \gamma^2 V_{20}(r, w_0). \end{aligned} \tag{2.35}$$

In the same way

$$V_{10}(r, \delta z_0) \simeq j\gamma V_{00}(r, w_0) + V_{10}(r, w_0)\left(1 + j3\gamma\right) + j2\gamma V_{20}(r, w_0). \tag{2.36}$$

At this point consider the case of the cavity matching. The parameters β and γ become

$$\beta = \frac{w_0^{(i)} - w_0^{(c)}}{w_0^{(i)}} \qquad \gamma = \frac{z_0^{(i)} - z_0^{(c)}}{2z_R^{(i)}}. \tag{2.37}$$

with index i which stands for the parameters of the input beam and c for the cavity parameters. Summing the Eq. 2.33 with 2.35 and 2.34 with 2.36 is possible to obtain the change-base matrix between laser base and the cavity one

$$V_{00}(r, w_0 + \delta w_0, \delta z_0) \simeq U_{00}(r, w_0 + \delta w_0) + U_{00}(r, w_0, \delta z_0) \simeq \tag{2.38}$$

$$\simeq U_{00}(r, w_0)\left(1 + j\gamma - \frac{\beta^2}{2} - \gamma^2\right) + U_{10}(r, w_0)\left(j\gamma - \beta + \frac{\beta^2}{2} - 2\gamma^2\right) + \tag{2.39}$$

$$+ U_{20}(r, w_0)\left(\beta^2 - \gamma^2\right)$$

and

$$\begin{aligned} V_{10}(r, w_0 + \delta w_0, \delta z_0) &\simeq U_{00}(r, w_0 + \delta w_0) + U_{00}(r, w_0, \delta z_0) \simeq \\ &\simeq U_{00}(r, w_0)\left(j\gamma + \beta\right) + U_{10}(r, w_0)\left(1 + j3\gamma\right) + U_{20}(r, w_0)\left(j2\gamma - 2\beta\right). \end{aligned} \tag{2.40}$$

Chapter 3

Mode match sensing

3.1 RF sensing technique

Let's consider a system where there is a mismatch between the laser beam and the optical cavity; expressed in the base of the cavity, the input beam will have components corresponding to higher order modes; if the carrier is resonant, in general the HOM will not, and will be mostly reflected annmariamthomas.

Using a particular device is possible to generate two modulated sidebands at the frequencies $\omega \pm \Omega$. The interference between these sidebands and the carrier at frequency Ω produces a modulation, which gives rise to a beat signal that can be detected. The laser beam is modulated in a way that the sideband $\omega+\Omega$ is resonant. The detected beat signal between the sidebands and the carrier component Ω is then demodulated in the in-phase and quadrature components. By a proper phase changing of the quadratures is possible to obtain two isolated error signals on the mismatch in waist size and position. Optically this device operates as a lens modifying the input beam and the differences in waist size and position between the modulated beam and the input one can be described as follow

$$\begin{aligned} \frac{\delta w_0}{w_0^i} &= B = \frac{m_B}{2}\left(e^{j\Omega t} + e^{-j\Omega t}\right) \\ \frac{\delta z_0}{2z_R^i} &= G = \frac{m_G}{2}\left(e^{j\Omega t} + e^{-j\Omega t}\right). \end{aligned} \tag{3.1}$$

Using 2.38 and limiting to the first order expansion it is possible to rewrite the modulated beam in its own basis

$$V(r,z) = (1+jG)V_{00}(r,z) + (jG - B)V_{10}(r,z). \tag{3.2}$$

To reach the cavity the beam propagates for a distance z_c accumulating a Gouy phase given by 2.5. In the cavity base, the resulting input complex amplitude could be express as

$$\begin{aligned} V(r,z_c) =& (1+jG)((1+j\gamma)U_{00}(r,z_c) + (j\gamma - \beta)U_{10}(r,z_c)) + \\ &+(jG - B)((j\gamma+\beta)U_{00}(r,z_c) + (1+j3\gamma)U_{10}(r,z_c) + (j2\gamma - 2\beta)U_{20}(r,z_c))e^{j\Delta\phi}. \end{aligned} \tag{3.3}$$

Keeping only first order terms in γ and β of 2.38 and remembering that the electric field of a monochromatic wave of frequency ω is given by the complex amplitude multiplied by $\exp[j\omega t]$ it follows:

$$\begin{aligned} \tilde{E} &= E_0 V(r,z_c)e^{j\omega t} = \\ &= E_0\left((1+j(\gamma+G))V_{00}(r,z_c) + (j(\gamma + Ge^{j\Delta\phi}) - (\beta + Be^{j\Delta\phi})V_{01}(r,z_c)\right)e^{j\omega t}. \end{aligned} \tag{3.4}$$

The reflected field from the cavity is obtained by the product of the incident field with the reflection transfer function:

$$V_{00}^{(r)} = (1+j(\gamma+G))e^{j\omega t}\otimes F(\omega) = F_{00}(\omega)(1+j\gamma)e^{j\omega t}+jF_{00}(\omega+\Omega)\frac{m_G}{2}e^{j(\omega+\Omega)t}+jF_{00}(\omega-\Omega)\frac{m_G}{2}e^{j(\omega-\Omega)t} \tag{3.5}$$

and similarly

$$V_{10}^{(r)} = \left(j\left(\gamma+Ge^{j\Delta\phi}\right)-\left(\beta+Be^{j\Delta\phi}\right)\right)e^{j\omega t}\otimes F_{01}(\omega) = \tag{3.6}$$

$$= F_{01}(\omega)(j\gamma-\beta)e^{j\omega t}+F_{01}(\omega+\Omega)\left(j\frac{m_G}{2}-\frac{m_B}{2}\right)e^{j\Delta\phi}e^{j(\omega+\Omega)t}+ \tag{3.7}$$

$$+F_{01}(\omega-\Omega)\left(j\frac{m_G}{2}-\frac{m_B}{2}\right)e^{j\Delta\phi}e^{j(\omega-\Omega)t}.$$

For completeness

$$F_{pl}(\omega) = \frac{r_1 - r_2(r_1^2+t_1^2)\exp\left[-j\left(\frac{\omega}{\Delta\omega_{FSR}}+N\phi_{rt}\right)\right]}{1-r_1r_2\exp\left[-j\left(\frac{\omega}{\Delta\omega_{FSR}}+N\phi_{rt}\right)\right]} \tag{3.8}$$

with LG order number N and ϕ_{rt} the Gouy phase accumulated after a round-trip.

In general the normalized reflected intensity of the reflected field is

$$\frac{I^{(r)}}{I_0} = \frac{\left|V_{00}^{(r)}\right|^2+\left|V_{10}^{(r)}\right|^2}{\left|E_0\right|^2} = \tag{3.9}$$

$$= -jF_{00}(\omega)F_{00}^*(\omega+\Omega)(1+j\gamma)\frac{m_G}{2}e^{-j\Omega t}+c.c.+ \tag{3.10}$$

$$-jF_{00}(\omega)F_{00}^*(\omega-\Omega)(1+j\gamma)\frac{m_G}{2}e^{j\Omega t}+c.c.+$$

$$+F_{10}(\omega)F_{10}^*(\omega+\Omega)(j\gamma-\beta)\left(-j\frac{m_G}{2}-\frac{m_B}{2}\right)e^{-j\Delta\phi}e^{-j\Omega t}+c.c.+$$

$$+F_{10}(\omega)F_{10}^*(\omega-\Omega)(j\gamma-\beta)\left(-j\frac{m_G}{2}-\frac{m_B}{2}\right)e^{-j\Delta\phi}e^{j\Omega t}+c.c.$$

Considering now the case where one of the two sidebands, for example the one at frequency $\omega+\Omega$, is perfectly resonant with LG01 mode of a perfectly matched cavity. The assumption of a perfectly matched cavity is made for simplicity of calculation, however it works in more general cases. The reflection transfer functions at the resonant frequencies becomes

$$F_{00}(\omega) = F_{10}(\omega+\Omega) = 0 \tag{3.11}$$

and for the non-resonant frequency

$$F_{10}(\omega) = F_{10}(\omega-\Omega) = 1. \tag{3.12}$$

After some simple math steps, the reflected intensity becomes

$$\frac{I^{(r)}}{I_0} = (\gamma m_G+\beta m_B)\cos(\Omega t-\Delta\phi)+(\beta m_G-\gamma m_B)\sin(\Omega t-\Delta\phi). \tag{3.13}$$

Therefore the two components read by the photodiode, after demodulation, have amplitudes:

$$\begin{aligned} I_Q &= I_0(\gamma m_G+\beta m_B) \\ I_I &= I_0(\beta m_G-\gamma m_B) \end{aligned} \tag{3.14}$$

which are the in-phase and quadrature error signals. From the above system is imediate to find an expression of γ and β as a function of the error signals

$$\begin{aligned} \gamma &= \frac{m_G I_Q - m_B I_I}{I_0(m_G^2+m_B^2)} \\ \beta &= \frac{m_G I_I + m_B I_Q}{I_0(m_G^2+m_B^2)}. \end{aligned} \tag{3.15}$$

The I and Q module becomes

$$MOD_{IQ} = \sqrt{(\gamma^2 + \beta^2)\left(m_G^2 + m_B^2\right)} \tag{3.16}$$

and finally the total mode-mismatch between the input laser beam and the cavity is defined as

$$MM = \sqrt{\gamma^2 + \beta^2}. \tag{3.17}$$

3.2 Electro-optical lens

The purpose of this thesis work is based on the design and study of the correct functioning of two electro-optical lens prototypes. Both EOL are modulating suitable devices based on a lithium niobate crystals enclosed by some suitable electrodes. These electrodes, exploiting the Pockels effect via a RF signal, induce the crystal to behave like a lens, generating radiofrequency sidebands in the LG10 or HG02 modes on the main beam. The effects that these devices produce on a laser beam interacting with an optical cavity can be read by photodetectors. In particular, looking at the reflected field from the cavity, is possible to online ectract a signal proportional to the mismatch [20].

3.2.1 Pockel effect

The functioning of an EOL is based on the electro-optical (or Pockel) effect: an electric field, applied to a lithium niobate ($LiNbO3$) crystals, is able to alter its index of refraction. Since the refractive index of a lens determines its focal length, modifying the electric field applied to the EOL device is possible to change waist sizes and positions of the outgoing laser beam. By continuously varying the beam waist in such a manner, the device can modulate a laser beam at radio frequencies.
Ferroelectric lithium niobate is a human-made dielectric material and is one of the most widely used electro-optic materials because of its large-magnitude physical effects. This material has a trigonal crystal structure and is naturally birefringent. It is characterized by large pyroelectric, piezoelectric, electro-optic and photoelastic coefficients [22] [4].

For a quantitative description of the electro-optical modulation effect is necessary to introduce a geometric construction called the index ellipsoid. If the axes of the ellipsoid correspond to the principal axes of the medium, its dimensions along these axes are the principal refractive indices

$$\frac{x_1^2}{n_1^2} + \frac{x_2^2}{n_2^2} + \frac{x_3^2}{n_3^2} = 1. \tag{3.18}$$

The latter equation can be rewritten in a bilinear form

$$\frac{1}{\eta_{ij}} x_i x_j = 1 \tag{3.19}$$

with η_{ij} a dielectric (or impermeability) tensor.

When a steady electric field $\vec{E}$ is applied to a crystal, the elements of the dielectric tensor are altered and each elements of it becomes a function of the electric field, so that the index ellipsoid is modified. Expanding η_{ij} in a Taylor series around $\vec{E} = 0$

$$\eta_{ij}(\vec{E}) = \eta_{ij}(\vec{0}) + \sum_k r_{ijk} E_k + \sum_{kl} s_{ijkl} E_k E_l \quad i,j,k,l = 1,2,3 \quad r_{ijk} = \frac{\partial \eta_{ij}}{\partial E_k} \quad s_{ijkl} = \frac{1}{2}\frac{\partial^2 \eta_{ij}}{\partial E_k \partial E_l}. \tag{3.20}$$

For the Pockels effect, this change has a linear dependence from the electric field

$$\Delta\left(\frac{1}{\eta_{ij}}\right) = r_{ijk} E_k \tag{3.21}$$

where r_{ijk} is the electro-optic tensor. Because η is symmetric, r is invariant under permutations of the indices i and j. Because of this permutation symmetry, the indices i and j generate six instead of nine independent elements. Consequently, r_{ijk} has 6×3 indepentent elements.
The symmetry of the crystal adds further constraints to the elements of the two derivative matrices. In particular, a trigonal crystal, such as the ferroelectric lithium niobate, is uniaxial, i.e. has $n_1 = n_2 = n_o$ called ordinary refraction index and $n_3 = n_e$ called extraordinary refraction index. The matrix r in this case gives

$$r = \begin{pmatrix} 0 & -r_{22} & r_{13} \\ 0 & r_{22} & r_{13} \\ 0 & 0 & r_{33} \\ 0 & r_{51} & 0 \\ r_{51} & 0 & 0 \\ -r_{22} & 0 & 0 \end{pmatrix}. \tag{3.22}$$

Assuming that the applied electric field points along the optics axis, $\vec{E} = (0, 0, E)$, the modified ellipsoid gives

$$\frac{x_1^2 + x_2^2}{n_o^2(E)} + \frac{x_3^2}{n_e^2(E)} = \left(\frac{1}{n_o^2} + r_{13}E\right)(x_1^2 + x_2^2) + \left(\frac{1}{n_e^2} + r_{33}E\right)x_3^2 = 1. \tag{3.23}$$

Now, using the Taylor-series approximation, one obtains

$$\begin{aligned} n_1 = n_2 = n_o(E) &\simeq n_o - \frac{1}{2}n_o^3 r_{13}E \\ n_3 = n_e(E) &\simeq n_e - \frac{1}{2}n_e^3 r_{33}E \end{aligned} \tag{3.24}$$

where the electooptics coefficients measure $r_{13} = 9.6\, pm/V$ and $r_{33} = 30.9\, pm/V$ and the refractive indices $n_0 = 2.176$ and $n_e = 2.2457$ at $0.633\, nm$. Fig. 3.1 shows how an uniaxial crystal is modified by an electric field applied along its optical axis: in particular is easy to see that the crystal remains uniaxial with the same principal axes.

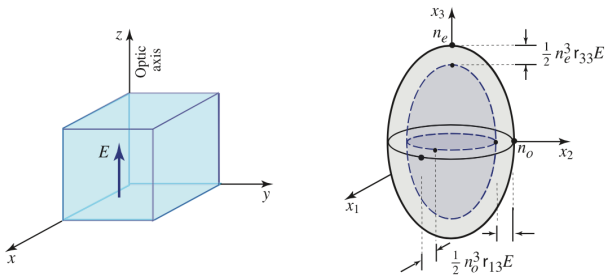

Figure 3.1: Modification of the index ellipsoid for a trigonal crystal while applying a steady electric field along the direction of the optic axis [18].

Electro-optical modulation

In the next chapter it will be described the experimental setup which includes three Lithium Niobate crystals: one Electro-Optic Modulator (EOM) and two custom built Electro-Optic Lenses.

Let's briefly analyze the functioning of the simplest type of EOM. A laser beam polirized in one of the ordinary crystal axes (for example x_1) interacts with a crystal with an applied electric field directed along $\hat{z}$, a change in the electric field induces a phase shift on the output beam

$$E_{EOM}(x,t) = E_0 \exp\left[kx - \omega_0 t + \Delta\alpha(t)\right] + c.c. \qquad \Delta\alpha(t) = k\Delta n(t) l = k\frac{n_e^3}{2} r_{33} E_z(t) l \tag{3.25}$$

with l the length of the crystal. Now consider the applied electrical field periodically varying over time $E_z(t) = E_z(0)\cos(\Omega t)$. Usually the phase shift of an high quality EOM is a really small value that can be treated as a perturbation and it is possible to apply Taylor

$$E_{EOM}(x,t) \simeq E(\omega t)(1 + j\Delta\alpha(\Omega t)) = E(\omega t)\left(1 + \frac{j\Delta\alpha(0)}{2}\left(e^{j\Omega t} + e^{-j\Omega t}\right)\right). \tag{3.26}$$

In addition to the initial laser beam field at frequency ω, two side bands of frequencies $\omega + \Omega$ and $\omega - \Omega$ have appeared.

The EOM modulates an input beam at radio-frequency generating two sidebands at frequency $\nu_{FSR} \pm \Omega/2\pi$. Instead the two EOLs will produce sidebands in LG10 or HG02 and HG20 modes; this is possible by applying a spatially non-uniform electric field.

A novel mode matching sensing technique

Now a novel high-sensitivity method to characterize and improve mode matching into optical cavities will be described. The technique is based on an electro-optical device which is able to produce a quadratic phase gradient on a laser beam, i.e. 45° rotated Hermite-Gauss mode (HG11). Thanks to the use of a mode converter telescope, an optical configuration made up of two cylindrical lenses, it is possible to convert the saddle wavefront in a Laguerre-Gauss bullseye mode (LG01). The generated sidebands of higher order modes produce a beat signal with the carrier field reflected by the cavity which contains information on the amount and type of mismatch [16] [10].

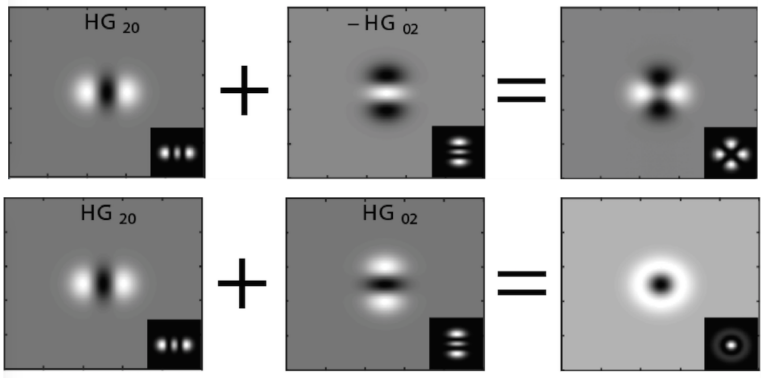

Figure 3.2: Beam decomposition of the $|HG_{11}^{45^\circ}>$ (a) and $|LG_{01}>$ (b) mode in the HG basis. Shown are the (real) field amplitudes of the two relevant HG modes (left) and the resulting modes (right). The intensity profile for each field is plotted in the bottom right corner for each field image [13].

To mathematically understand how this conversion works, let's decompose an initial beam with a hyperbolic saddle point wave front in the $|HG_{nm}>$ basis

$$|HG_{11}^{45^\circ}> = \frac{1}{\sqrt{2}}|HG_{20}> - \frac{1}{\sqrt{2}}|HG_{02}>. \tag{3.27}$$

On the contrary the parabolic wave front beam, i.e. bullseye mode, in the same basis yields

$$|LG_{01}> = \frac{1}{\sqrt{2}}|HG_{20}> + \frac{1}{\sqrt{2}}|HG_{02}>. \tag{3.28}$$

This means that the only difference between the two modes is a sign flip along one axis.

Using an astigmatic telescope composed by two cylindrical lenses is possible to obtain the desire effect. Let's use the ray matrix method, calling S and T rispectively the sagittal and tangential plane orthogonal to the beam direction

$$M_S = \begin{pmatrix} 1 - \frac{l}{f_1} & l \\ \frac{1 - f_1 - f_2}{f_1 f_2} & 1 - \frac{l}{f_2} \end{pmatrix} \qquad M_T = \begin{pmatrix} 1 & l \\ 0 & 1 \end{pmatrix} \tag{3.29}$$

with l the distance between the lenses and $f_{1,2}$ their focal lengths. Now using Eq. 2.9 the extra Gouy phase induced by the telescope becomes

$$\Delta\psi_{nm} = \left(n + \frac{1}{2}\right)\psi_T + \left(m + \frac{1}{2}\right)\psi_S \quad \text{with} \quad \psi_{S,T} = Arg[C_{S,T}q_i + D_{S,T}]. \tag{3.30}$$

A $\pi/2$ mode converter creates a region where Gouy phase is accumulated at different rates for each of the transverse axis. Since second order modes accumulate twice the Gouy phase, the $|HG_{20}>$ and the $|HG_{02}>$ have a phase difference of π which, via the Euler identity $-1 = e^{j\pi}$, confirmed the sign flipping between the two decompositions. Mathematically

$$\Delta\psi_{02} - \Delta\psi_{20} = -2(\psi_T - \psi_S) = \pi. \tag{3.31}$$

Since $C_T = 0$, $\psi_T = 0$ and so $\psi_S = \pi/2$.
Moreover we have to impose that the beam after the telescope has the same Kogelnik parameters in the two planes $q_S = q_T$, i.e. the two HG mode has to be re-matched.
Imposing for simplicity $f_1 = f_2 = f$ the focal length entirely defines the beam parameters and the position of the lenses. The conditions thus obtained are:

$$l = \sqrt{2}f \tag{3.32}$$

$$z - z_0 = \frac{l}{2} \tag{3.33}$$

$$w_0 = \sqrt{\left(1 + \frac{1}{\sqrt{2}}\right)\frac{\lambda f}{\pi}}.$$

3.2.2 EOL-Pd

The first EOL device is made of a *sandwich* of two biconcave electrodes that enclose a Lithium Niobate crystal in between. This device is designed to behave as a lens that can change its refraction index, proportionally to the voltage applied to its electrodes. For a more in-depth analysis of this apparatus, see [17].
The substrate used for this porpuse is essentially a parallelepiped with dimensions $2 \times 0.8 \times 0.5\,cm$ so that the longer side is placed along the laser beam propagation direction. The electrodes are collocated at the end of the larger surfaces so that the electric field in the sample is directed along the vertical axis (see Fig 3.3). Optically the electro-optical device's effect can be compared to the one of a spherical lens with focal length

$$f_{\text{EOL-Pd}} = 8.3 \cdot 10^3\, m \tag{3.34}$$

and propagation through a medium with index of refraction

$$n_{EOL} = 2.23. \tag{3.35}$$

Therefore the idea behind this project is to realize a device that can induce RF modulation of the beam mode LG10.

3.2.3 EOL-Fl

The concept for the second EOL was developed initially by Mauricio Diaz-Ortiz Jr and Paula Fulda from the University of Florida and subsequently modified by the PhD student G. Chiarini. The idea is similar to the EOL-Pd, i.e. a Lithium Niobate crystal enclosed by some electrodes. What changes is the geometry of the electrodes and the consequent lens effect of the crystal on the laser beam. The *sandwich* now is composed by six rectangular electrodes, three above and three below the crystal, with alternating polarity: this configuration is able to produce a quadratic phase gradient, which results

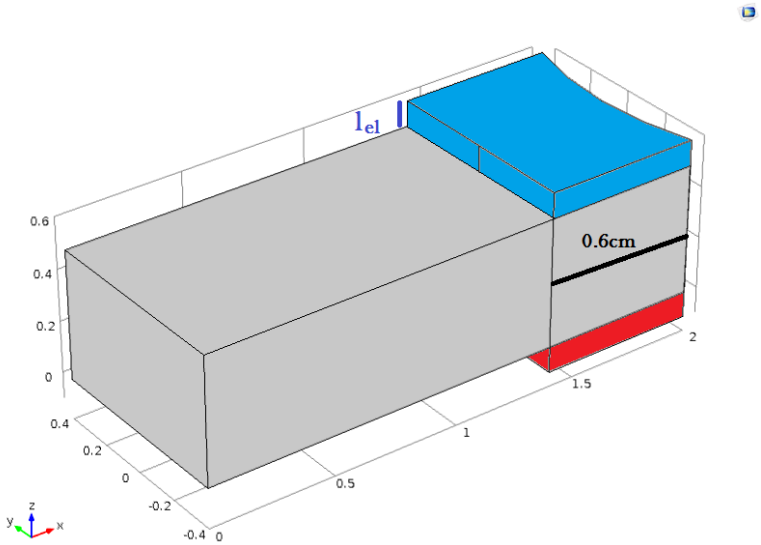

Figure 3.3: Graphic representation of the EOL-Pd geometery modeled by COMSOL Multiphysics software for finite element analysis. In this case the laser beam is directed along the x axis, from left to right.

in a saddle effect on the laser wavefront. Therefore the final effect of the device is to induce RF modulation of the beam mode HG11 rotated by an angle of 45° [13].

Optically this particular device must produce an antisymmetric effect in the two directions orthogonal with respect to the laser beam propagation axis. In other words, the diopters in $\hat{y}$ and $\hat{z}$, consequently the optical paths or focal lengths, must be equal and opposite. In particular,

$$f^{(y)}_{\text{EOL-Fl}} \simeq -30\,m \qquad f^{(z)}_{\text{EOL-Fl}} = 30\,m. \tag{3.36}$$

COMSOL Multiphysics software for finite element analysis was used to find the optimal geometry for the electrodes: four copper electrodes with dimensions $10 \times 2 \times 0.5\,mm$ and two smaller one with dimensions $7 \times 2 \times 0.5\,mm$. Thanks to the use of a 3D printer, a plastic case was created to contain the electrodes and the crystal. Fig. 3.5 shows the final result of the construction process.

3.3 EOL testing

An optical cavities to be stable has to satisfy the following conditions: the laser frequency matches the cavity resonance frequency and the laser beam wavefront matches the curvature of the cavity reflection mirror. Failure in meeting the second condition, the geometric condition, is called mode mismatch.

The EOL device can alter the laser waist by applying a varying electric fields to the crystal. The modulation it induces is similar to the Pound-Drever-Hall locking scheme for frequency stabilization. The device generates one resonant and one non-resonant sideband around the carrier signal at the MHz frequency. The light is modulated at a frequency Ω such that the LG01 sideband with frequency $\omega + \Omega$ is resonant and completely transmitted into the cavity. If some mode mismatch is present, then the carrier has a component that couples to the higher-order modes of the cavity and will be reflected off from the cavity. Demodulating in the I and Q quadratures the detected beat signal between this component and the non-resonant sideband provides the error signal for mode mismatch which quantifies how different the beam waist is with respect to the waist required by the cavity [**?**].

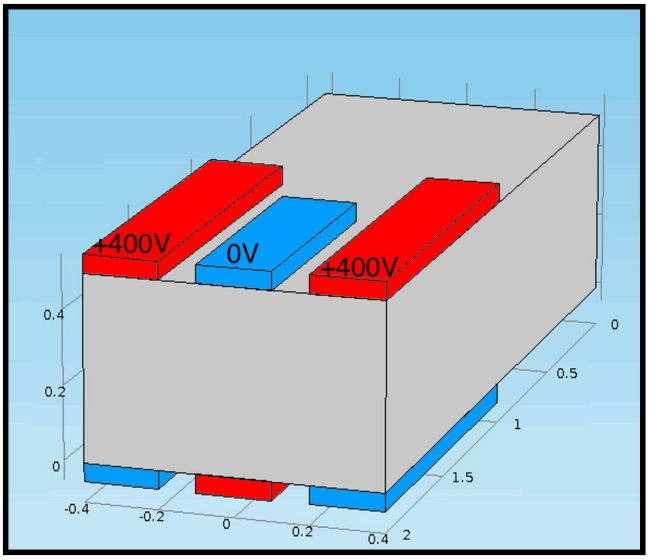

Figure 3.4: Graphic representation of the EOL-Fl geometery modeled by COMSOL Multiphysics software for finite element analysis. In this case the laser beam is directed along the x axis, from left to right.

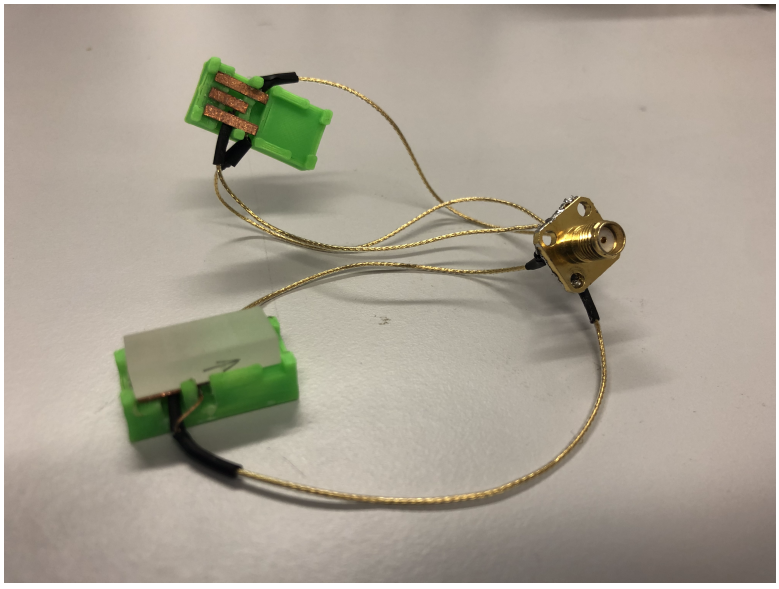

Figure 3.5: Photo of the final result of the construction process. In addition to the green case, the electrodes and the crystal, note the coaxial connector to which the various cables have been soldered.

Chapter 4

Experimental setup

To implement the investigated RF mode sensing technique an experimental setup has been built before this thesis work in Laboratori Nazionali of Legnaro (INFN-LNL) [17] [6]. In this chapter it will be analyze the implementation of two different EOL for two configurations of the same experimental setup. After that two technique for mode mismatch sensing will be presented: analysis of the modes inside a triangular cavity and wavefront differential measurements.

4.1 Optical table

To study the effects of the firts EOL device, called EOL-Pd, on the optical table, another optical line is implemented that allows to analyze the beam variations, leaving unchanged the alignment with the cavity. To do that a beamsplitter 70/30, labeled M_{16}, is positioned between the mode-matching telescope $L_6 - L_7$ and the triangular cavity (see Fig.4.1). At this point two subsequent mirrors (M_{17} and M_{18}) direct the beam onto a free area of the optical bench. Finally another telescope ($L_9 - L_{10}$) prepares the beam for the wavefront sensor.

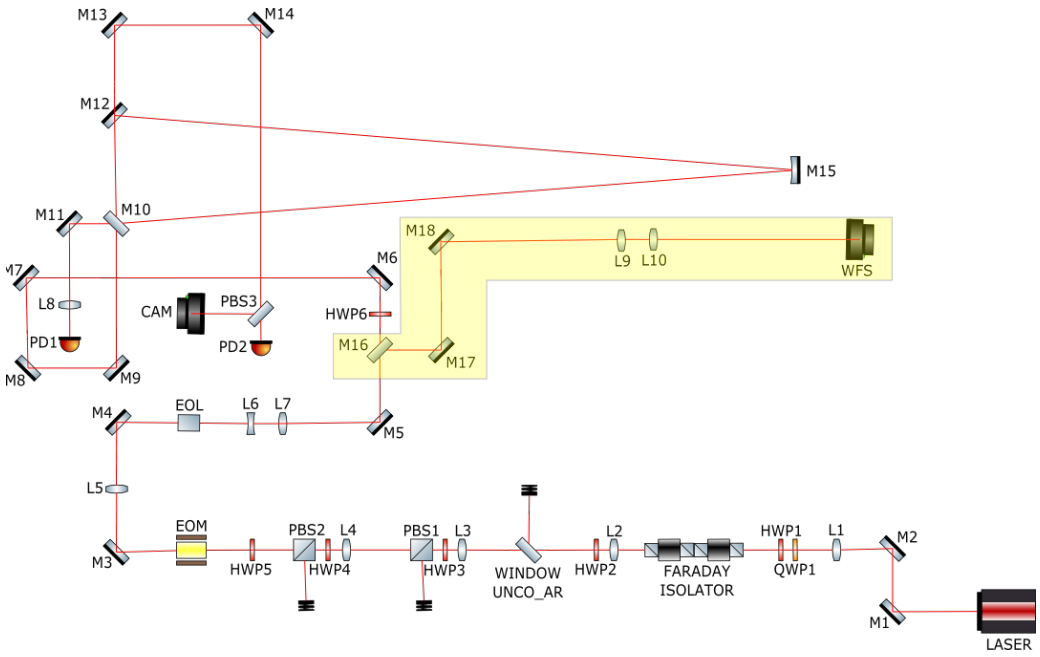

Figure 4.1: First optical bench scheme. The laser source is a Nd:Yag crystal that emits light at 1064 nm. The Faraday isolator is used to prevent the back-reflection of light towards the laser. The EOM is used for the stabilization of the cavity. The light reflected off from the triangular optical cavity is detected by PD1 and the transmitted light by PD2. In yellow the new optical line implemented.

To determine the optics necessary for the optical setup it is essential to study the beam parameters through analytical calculations with the use of ray-transfer matrix method. Defining as $\hat{z}$ the laser beam propagation axis, the zero reference (i.e. $z = 0$) for all the rest of the discussion will be the lens position z_5. The parameters of the initial beam after L_5 are already known

$$\begin{aligned} w_0^{(x)} &= 438\,\mu m \qquad & z_0^{(x)} &= 35.8\,cm \\ w_0^{(y)} &= 405\,\mu m \qquad & z_0^{(y)} &= 36.6\,cm. \end{aligned} \tag{4.1}$$

Using Eq. 3.17 is possible to measure the mismatch between the beam parameters in the two orthogonal directions

$$MM \simeq 8\% \tag{4.2}$$

a small value of it justifies the possibility of taking the average of 4.1

$$w_0^{(i)} = 421.5\,\mu m \qquad z_0^{(i)} = 36.2\,cm. \tag{4.3}$$

A triangular optical cavity is used in place of a linear cavity due to limitations in space. It consists in two flat mirrors and a curved mirror. The cavity is impedance matched with

$$\Delta\nu_{FSR} = 83.3\,MHz \qquad \Delta\nu_{HM} = 686.8\,kHz \qquad \mathcal{F} = 386.5. \tag{4.4}$$

The cavity parameters are the following

$$\text{length} = L = 180.163\,cm \qquad R_1 = +\infty \qquad R_2 = 600\,cm \tag{4.5}$$

using the formula for the g-parameter

$$g_{1,2} = 1 - \frac{L}{R_{1,2}} \tag{4.6}$$

gives

$$w_0^{(cav)} = \left[\left(\frac{L\lambda}{\pi}\right)^2 \frac{g_1 g_2(1 - g_1 g_2)}{(g_1 + g_2 - 2g_1 g_2)^2}\right]^{1/4} \simeq 965\,\mu m \tag{4.7}$$

The waist position is in the center of the short side of the cavity, that is, between M_{10} and M_{12}, which are 15 cm away from each other. The waist position becomes

$$z_0^{(cav)} \simeq 2\,m. \tag{4.8}$$

After positioning the electro-optical lens at position $z_{EOL-Pd} = 30\,cm$ a suitable optical telescope has been studied to match the cavity parameter using a software called Just Another Mode Matching Tool (JamMT). This graphis interface software allows to calculate, through ABCD matrices, the outgoing beam from a given optical system, knowing the input parameters and the characteristics of the optical components that constitute the optical setup. Using the modematching tool in JamMt it is possible to obtain different telescope options for cavity modematching. The best configuration, which mimimize the mismatch and takes into account the real space available on the optical bench, yields a lens L_6 of $f_6 = -112\,mm$ at $z_6 = 423\,mm$ and L_7 of $f_7 = 280\,mm$ at $z_7 = 604\,mm$. The values of the focal lengths in this case are already the result of the sum of their nominal values plus a correction of 12%, obtained using the general focal length's formula

$$\frac{1}{f} = (n-1)\left[\frac{1}{R_1} - \frac{1}{R_2} + \frac{(n-1)d}{nR_1R_2}\right] \tag{4.9}$$

where n is the refractive index of the lens medium, $R_{1,2}$ the radii of curvature and d the thickness.

At this point, considering the space available on the optical bench, on which other experiments are placed, M_{16} is inserted at $z_{16} = 77.5\,cm$ from M_5. The beam parameter at the beamsplitter position

are obtained scanning the outgoing laser, previously aligned using M_{17} and M_{18}. The results of the beam scan are reported below:

$$w_0^{(x)} = 0.78 \pm 0.01\ mm \qquad z_0^{(x)} = 1690 \pm 50\ mm \tag{4.10}$$
$$w_0^{(y)} = 0.741 \pm 0.008\ mm \qquad z_0^{(y)} = 1450 \pm 30\ mm.$$

Considering the available space on the optical bench to place the wavefront sensor and using the beam parameters 4.10, a possible configuration found consists in a telescope with the first lens L_9 of $f_9 = 112\ mm$ at $z_9 = 1475\ mm$ and the second one L_{10} of $f_{10} = 336\ mm$ at $z_{10} = 1725\ mm$. The resulting beam has the following parameters

$$w_0^{(x)} = 75\ \mu m \qquad z_0^{(x)} = 707\ mm \tag{4.11}$$

The sensor is positioned at $z_{WFS} \simeq 1916\ cm$ and the beam at this distance is $W(z_{WFS}) \simeq 2.25\ mm$ wide.

4.1.1 Modification to integrate EOL-Fl

In order to be able to study the functioning of the two EOL, EOL-Pd and EOL-FL, a new version of the same optical setup (Fig. 4.2) is organized, consisting in a line with common optical components, and thanks to the presence of two flip mirrors (M_5 and M_8), gives the possibility to operate alternatively on the two EOL.

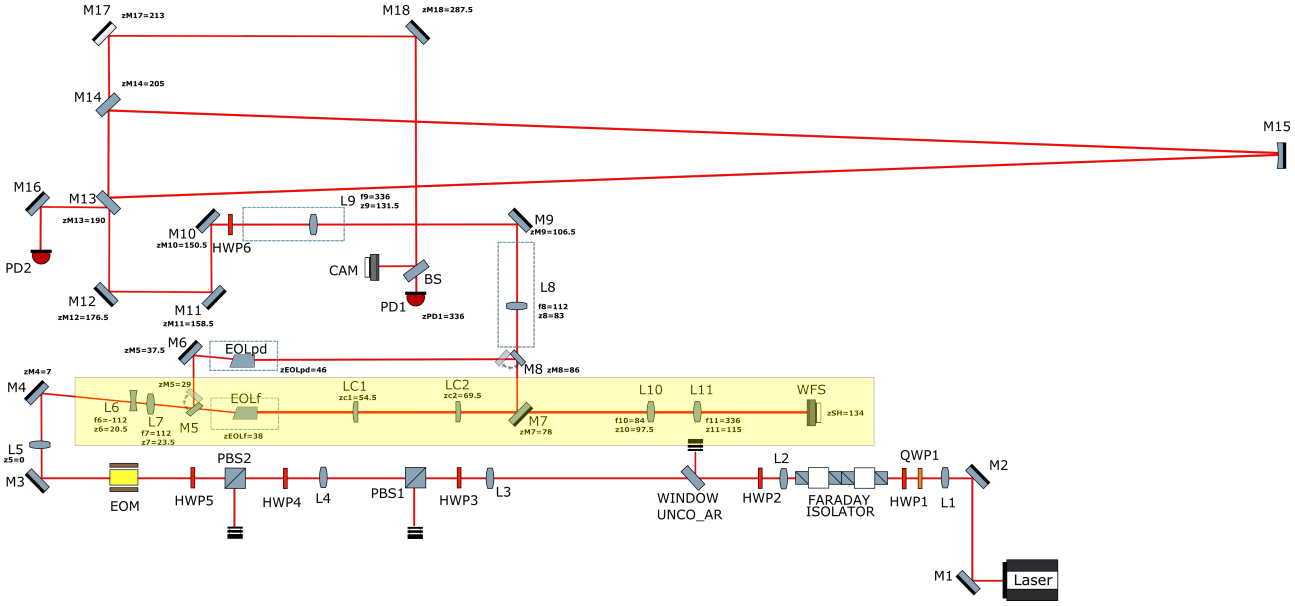

Figure 4.2: New configurations of the same experimental setup of Fig. 4.1. The optical components before L_5 are the same. In yellow the optical line described in the following section. The dashed rectangles represents the dedicated mount for the two EOL and the linear stages for L_8 and L_9.

The initial beam parameters after L_5 are the same of Eq. 4.1. Considering Sec. 3.2.1, an electro-optical device which is able to produce a quadratic phase gradient on a laser beam needs a mode converter telescope to work. In order to determine the positions of the cylindrical lenses (LC_1 and LC_2) of the mode converter telescope I have to impose the theoretical conditions of Eq. 3.32. In particular the fused silicia cylindrical lenses used for this aim have the following characteristics

$$n = 1.4496\ (@\ 1064\ nm) \qquad R_1 = 50.85\ mm \qquad R_2 \sim \infty \qquad d = 5\ mm. \tag{4.12}$$

Now using the general focal length's formula 4.9 it gives a value of $f_{cyl} \simeq 113\ mm$ and inserting it in 3.32

$$l_{cyl} \simeq 15.98\ cm \qquad w_0^{(cyl)} \simeq 255.6\ \mu m.$$

This means that the lenses will be positioned approximately at $z_{LC} = z_0^{(1)} \pm l_{cyl}/2$, being $z_0^{(1)}$ the waist position after the first telescope $(L_6 - L_7)$. Because of the necessity of having enough space to install a flip mirror and the EOL-Fl between the first mode matching telescope and the astigmatic one, I search with JamMT this configuration, finding

$$f_6 = -112\,mm \quad z_6 \simeq 20.5\,cm \quad f_7 = 112\,mm \quad z_7 \simeq 23.5\,cm. \tag{4.13}$$

The beam after this first telescope has the following parameters

$$w_0^{(1)} \simeq 252\,\mu m \qquad z_0^{(1)} \simeq 60\,cm. \tag{4.14}$$

Due to the inaccuracy of the positions of the various optical components on the optical bench, to establish the real positions of the cylindrical lenses is necessary to perform several beam scans, moving a bit the lenses, in order to minimize the astigmatism of the beam after of the mode converter telescope. The best fit obtained is for

$$z_{LC_1} \simeq 54.5\,cm \qquad z_{LC_2} \simeq 69.5\,cm \tag{4.15}$$

shown in the figure 4.3 and the resulting parameters are

$$\begin{aligned} w_0^{y(2)} &= (248 \pm 2)\mu m \quad z_0^{y(2)} = (62.0 \pm 0.6)cm \quad z_R^{y(2)} = (18.2 \pm 0.3)cm \\ w_0^{x(2)} &= (247 \pm 3)\mu m \quad z_0^{x(2)} = (61.7 \pm 0.9)cm \quad z_R^{x(2)} = (18.0 \pm 0.5)cm. \end{aligned} \tag{4.16}$$

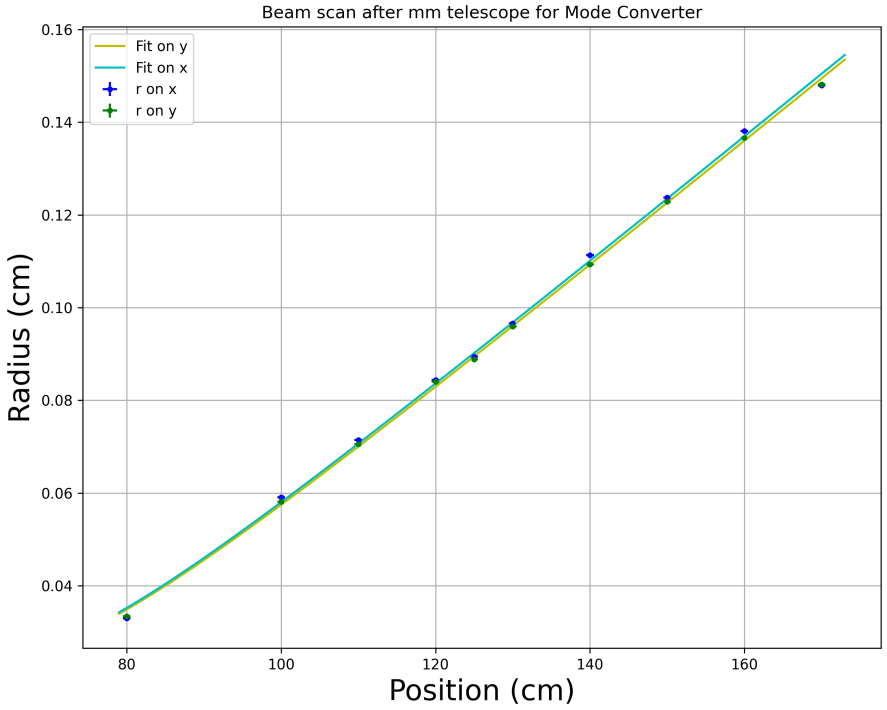

Figure 4.3: Beam scan fitting curve after the mode converter telescope. Because of the fluctuations of the measurements each waist measurement is the mean of 10 values.

A second mode matching telescope is installed to match the beam to the cavity. Also this time several configurations are studied with JamMT and the best solution gives

$$f_8 = 112\,mm \quad z_8 \simeq 83\,cm \quad f_9 = 336\,mm \quad z_7 \simeq 131.4\,cm. \tag{4.17}$$

The beam after this telescope has the following parameters

$$w_0^{(3)} \simeq 887\,\mu m \qquad z_0^{(3)} \simeq 193\,cm. \tag{4.18}$$

The total mismatch with the cavity gives $MM \simeq 8\%$.

For the sake of simplicity M_7 is removed to install a new telescope for the wavefront sensor consisting of the following optical components

$$f_{10} = 84\,mm \quad z_{10} = 97.5\,cm \quad f_{11} = 336\,mm \quad z_{11} = 115.0\,cm. \tag{4.19}$$

With the above optical setup, the position for the wavefront sensor gives $z_{WFS} \simeq 134.1\,cm$.

4.2 Optical cavity as mode analyzer

The effect of the EOL device can be characterized by scanning the optical cavity at varying frequencies of the laser light. As seen at the end of Sec. 2.3.1, each mode resonates at a different frequency, therefore the power of each resonant peak is a measure of the strength of the corresponding mode within the beam. The mode mismatch percentage in the optical setup is obtained by looking at the power of the 02 and 20 mode as a percentage of the 00 mode peak power while switching ON and OFF the device by sending an oscillating wave to it. In particular the EOL power supply signal consists in a square wav that oscillates between $0 - 400\,V$.

The instument which read the photodetected signal is called MOKU:lab: this instrument uses a FPGA to acquire, analyse, and generate signals. Its output is connected to a laser piezo actuation which it is used to control the laser frequency, for both cavity scan and PDH feedback loop.

4.3 Shack-Hartmann sensor for wavefront measurements

Another way to study the effects that the electro-optical device produces on a laser beam is through the use of a wavefront sensor, called Shack-Hartmann, which, in this particular case, will perform differential measurements of how the wavefront is modified by switching ON and OFF the EOL.

A Shack-Hartmann Wavefront Sensor (WFS) is a device based on a digital camera and a microlens array (MLA), able to privide measurements of the wavefront and the intensity distribution of optical beams. The operation principle consists in creating a matrix of focal spots on a camera sensor, which is mounted in the focal plane of the microlens array. In other words each lenslet collects the light incident to its aperture and generate a single spot on the sensor plane, then the WFS software analyzes the intensity and centroid locations of the focal spots, which indicate the field intensity and the orientation of the wavefront respectively averaged over the entrance area of the lenslet [21].

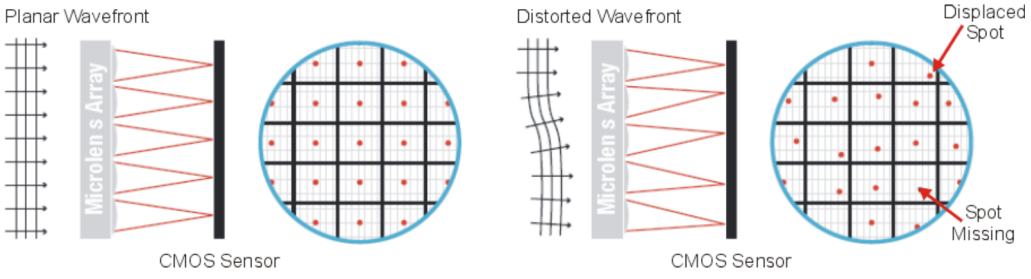

Figure 4.4: Operation principle of the microlens array which focuses a planar and a distorted wavefront [21].

Let's consider a distorted wavefront incident on the sensor: the focal spot has coordinates $(\delta x, \delta y)$ with respect to the corresponding reference coordinates, or reference spotfield, which corresponds to the coordinates of the spots if the incident wavefront is planar and parallel to the plane of the lenslets. Calling $W(x, y)$ the phase of the beam on the MLA plane, the partial derivatives in the plane orthogonal to the optical axis is determined by the spot shift

$$\frac{\partial}{\partial x} W(x,y) = \frac{\delta x}{f_{ML}} \qquad \frac{\partial}{\partial y} W(x,y) = \frac{\delta y}{f_{ML}} \tag{4.20}$$

where f_{ML} is the focal length of the microlens. The wavefront shape function is obtain by a 2-dimensional integration process of these spot deviations.

In general, the function describing an arbitrary wavefront in cartesian (or polar) coordinates, denoted by $W(x, y)$, can be expanded in terms of a sequence of Zernike functions $Z_n(x, y)$. These functions consist in a complete set of infinite number of polynomials, parametrized by two variables, that are orthogonal and continuous over the interior of a unit circle, or circular pupil

$$W(x, y) = \sum_{n=0}^{\infty} c_n Z_n(x, y). \tag{4.21}$$

with $c_n \in \mathbb{R}$ the Zernike amplitudes or coefficients, which weigh the contribution of each single polynomial and generally are determined by a least square Zernike fit. In Tab. 4.1 are reported the first ten Zernike coefficients and polynomials. Fig. 4.5 illustrates the wavefront aberrations for Zernike functions of order $0 - 7$ for all angular frequencies.

Nome	Mode	Order	Frequency	Norm	$Z_n(x, y)$	$Z_n(\rho, \theta)$
Piston	1	0	0	1	1	1
Tip y	2	1	-1	1	$\rho \sin[\theta]$	y
Tilt x	3	1	1	2	$\rho \cos[\theta]$	x
Astigmatism $\pm 45°$	4	2	-2	$\sqrt{6}$	$\rho^2 \sin[2\theta]$	$2xy$
Defocus	5	2	0	$\sqrt{3}$	$2\rho^2 - 1$	$2x^2 + 2y^2 - 1$
Astigmatism $0°/90°$	6	2	2	$\sqrt{6}$	$\rho^2 \cos[2\theta]$	$x^2 - y^2$
Trefoil y	7	3	-3	$\sqrt{8}$	$\rho^3 \sin[3\theta]$	$3x^2y - y^3$
Coma x	8	3	-1	$\sqrt{8}$	$3\rho^3 \sin[\theta] - 2\rho \sin[\theta]$	$3x^2y + 3y^3 - 2y$
Coma y	9	3	1	$\sqrt{8}$	$3\rho^3 \cos[\theta] - 2\rho \cos[\theta]$	$3x^3 + 3xy^2 - 2x$
Trefoil x	10	3	3	$\sqrt{8}$	$\rho^3 \cos[3\theta]$	$x^3 - 3xy^2$

Table 4.1: Zernike polynomials in polar and cartesian coordinates of order $0 - 3$.

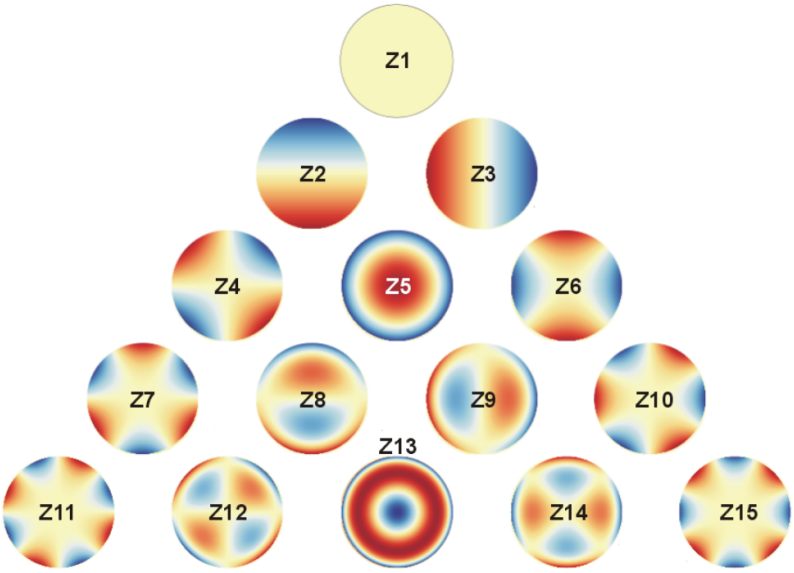

Figure 4.5: Wavefront aberration for Zernike functions [21].

The wavefront parameters (e.g. the beam center or diameter) are calculated over the entire selected sensor area, while the Zernike functions are calculated only for the area of a user-defined pupil. The pupil defines a circular area within the spot field. Since all Zernike functions are defined within the unic circle, only the spots located within the pupil area are used for fitting the measured wavefront to Zernike functions. For a Gaussian beam shape the pupil diameter is usually set to its width (see Eq. 2.5).

The camera image size defines the acrive area used for wavefront measurements. The smaller the image size, the fewer spots are used for calculation and the lower maximum achievable Zernike order. On the other hand, measurement speed increases. This means that to correctly measure higher order wavefront terms up to a certain Zernike order, it requires a minimum number of detected microlens spots. Fig. 4.6 shows the possible camera resolutions for the sensor used in this thesis work, i.e. Thorlabs' Shack-Hartman WFS30-5C. The minimum camera resolution $360 \times 360\ px$ corresponds to an aperture of $2.11 \times 2.11\ mm$ and being the sensor filled by a $150\ \mu m$ microlenses, this mean $13 \times 13 = 169$ spots count. Moreover the accuracy and the sensitivity associated at each wavefront measurement, for the just mentioned device, are respectively $\lambda/25$ and $\lambda/80$ at $633\ nm$.

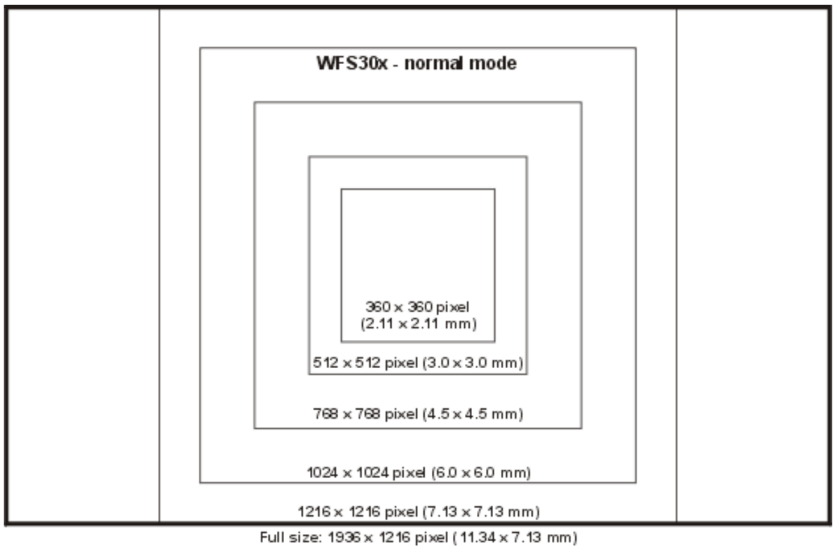

Figure 4.6: Selectable camera image sizes for WFS30 [21].

4.3.1 Defocus

The defocus corresponds to the fifth Zernike mode and it is directly linked to the radius of curvature, i.e. a parameter that describes the degree of curvature of the measured wavefront. In other words, the radius of curvature represents the distance between the reference plane of the WFS and the point source of the spherical wavefront. In polar coordinates

$$W(\rho) = c_5 Z_5(\rho) = c_5\sqrt{3}(2\rho^2 - 1) \tag{4.22}$$

with $\sqrt{3}$ the normalization factor (Tab. 4.1). Since the normalized radial coordinate ρ ranges from 0 to 1 and the spherical shape achieves its minimum and maximum wavefront deviation at these points, the peak to valley PV (Fig. 4.7) value is just the difference

$$PV = W(\rho = 0) - W(\rho = 1) = -2\sqrt{3}c_5. \tag{4.23}$$

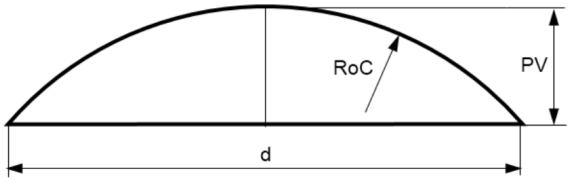

Figure 4.7: Peak to valley scheme.

One can assume a circle or radius of curvature RoC which gives the same PV value over the considered pupil. The sagitta formula in spherical coordinates gives

$$RoC = \frac{d_{pupil}^2}{8PV} + \frac{PV}{2} \simeq \frac{d_{pupil}^2}{8PV} \quad \text{because} \quad RoC \gg \frac{PV}{2} \tag{4.24}$$

with d_{pupil} the pupil diameter.

4.3.2 Conjugate plane discussion

In order to use the Shack-Hartmann sensor for the study of the wavefront, usually a telescope to modify the beam implemented . Considering Eq. 4.24, for a telescope with magnification factor M

$$RoC^{(out)} = M^2 RoC^{(in)} \rightarrow PV^{(out)} = \frac{1}{M^2} PV^{(in)}. \tag{4.25}$$

so, it means that to increase Δc_5, I have to decrease the magnification factor as much as possible, taking into account the minimal camera aperture of the WFS which is 2.11 mm (figure 4.6), it is decided to put the laser beam in the condition that its beam is slightly greater than the minimum selectable camera image size for the sensor.

EOL-Pd theoretical predictions

Using the dedicated Python program it is possible to obtain the theoretical values one expects via the ray-transfer matrix method and the sagitta formula. As said in Sec. 3.2.2 the effect of EOL-Pd, when switched ON, can be described by the product of two matrices: one describing the propagation inside the medium and the second one describing the transmission thorough a thin lens. For the numerical values of the refractive index and the focal length see Eq. 3.35 and 3.34. In the case of a magnification factor of $M \simeq 5$ (see Eq. 2.12) and computing all the values at z_{WFS}

$$\begin{aligned} &W_{OFF}^{(Pd)} \simeq 3.1147\, mm \quad RoC_{OFF}^{(Pd)} \simeq 417.6630\, mm \quad c_{5,OFF}^{(Pd)} \simeq -1.749530\, \mu m \quad PV_{OFF}^{(Pd)} \simeq 6.060548\, \mu m \\ &W_{ON}^{(Pd)} \simeq 3.1146\, mm \quad RoC_{ON}^{(Pd)} \simeq 417.6632\, mm \quad c_{5,ON}^{(Pd)} \simeq -1.749531\, \mu m \quad PV_{ON}^{(Pd)} \simeq 6.060552\, \mu m \end{aligned} \tag{4.26}$$

with pupil diameter $d_{\text{pupil}} = 4.5\, mm$. The theoretical differences are

$$\Delta W^{(Pd)} \simeq 0.08\, \mu m \quad \Delta RoC^{(Pd)} \simeq 2\, \mu m \quad \Delta c_5^{(Pd)} \simeq 1\, pm \quad \Delta PV^{(Pd)} \simeq 3\, pm. \tag{4.27}$$

EOL-Fl theoretical predictions

Using another time the same dedicated Python program is possible to obtain the theoretical predictions of the wavefront variations, with the difference that in this case the focal lengths of the resulting lens for EOL-Fl are given by Eq. 3.36

$$\begin{aligned} &W_{OFF}^{(Fl)} \simeq 1.181\, mm \quad RoC_{OFF}^{(Fl)} \simeq 287.1\, mm \quad c_{5,OFF}^{(Fl)} \simeq -0.5028\, \mu m \quad PV_{OFF}^{(Fl)} \simeq 1.741\, \mu m \\ &W_{ON}^{(Fl)} \simeq 1.183\, mm \quad RoC_{ON}^{(Fl)} \simeq 286.8\, mm \quad c_{5,ON}^{(Fl)} \simeq -0.5032\, \mu m \quad PV_{ON}^{(Fl)} \simeq 1.743\, \mu m. \end{aligned} \tag{4.28}$$

The theoretical differences are

$$\Delta W^{(Fl)} \simeq 3\, \mu m \quad \Delta RoC^{(Fl)} \simeq 0.3\, mm \quad \Delta c_5^{(Fl)} \simeq 1\, nm \quad \Delta PV^{(Fl)} \simeq 2\, nm. \tag{4.29}$$

Chapter 5

Measurements

Once the experimental setup and the theoretical expectations of the effect of the two EOLs on the laser wavefront have been presented, in this chapter the various measurement methodologies adopted and the results obtained will be described. As already mentioned in chapter 4, the methods used for the measurements are two: the first consists in measuring the variations on the laser wavefront by switching the electro-optical devices ON and OFF; the second consists in a modal analysis of the frequencies inside the triangular cavity, in particular how the height of the LG10 mode, excited by the mismatch (see Sec 2.4).

5.1 SH measurements

5.1.1 Methodology

In this first section will be presented the WFS's methodology and the results obtained. The Shack-Hartman wavefront sensor used in this thesis is able to acquire images in three different modes:

- Continuous mode: the camera operates in free running mode acquiring the images automatically and continuously.
- Software mode: the WFS application controls the image acquisition delating all buffered images at the start of each new exposure, and new images acquired by the camera are transferred to the PC.
- Trigger mode: in this mode the image acquisition is synchronized by an external trigger signal, which may be a pulsed laser source or an electrical function generator.

Since an extremely small variation of the wavefront is expected (see Sec. 2.2.1) it is not possible to carry out a direct measurement of the wavefront with EOL ON and OFF. To push the sensitivity of the instrument beyond its limit (see 4.3), I will try to carry out lock-in measurements with a large number of averages. For this porpuse it is used the trigger mode. In particular, through a common function generator (Keysight 33522A), two square waves are sent both to the investigated electro-optical device, as power supply, and to the WFS as trigger signal, after being suitably amplified (using a HV amplifier TREK model 2210 and a piezo amplifier PI E-413). The square waves are synchronized in such a way that the trigger frequency is exactly double that of the switching ON and OFF of the EOL. The trigger mode of the SH works in such a way that it acquires an image on the rising edge of the signal whenever the amplitude sent exceeds a certain threshold. Therefore, if you want to make measurements both in the ON and OFF phases of the EOL, you will need a trigger frequency double with respect to the power supply. Fig. 5.1 shows a screenshot of the MOKU:lab device in oscilloscope mode where is possible to see the two signals sent to the devices.

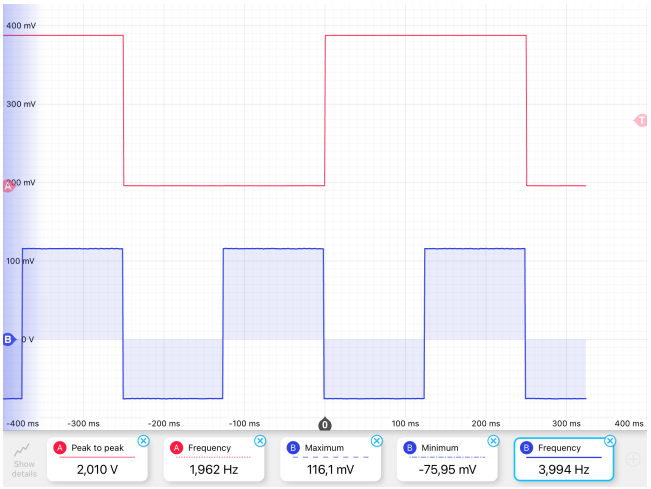

Figure 5.1: MOKU:lab screenshot in oscilloscope mode. In red the signal sent to the EOL as power supply and in blue the trigger signal sent to the WFS.

A dedicated LabVIEW program writes on a text file the values of the first ten Zernike coefficients and the time elapsed between one measurement and the next one. Taking some measurements in continuous mode it can be seen that the time between one measurement and the next, i.e. the program execution time, is $\simeq 125\,ms$; this imposes a lower limit for the trigger frequency of $\simeq 8\,Hz$. If the trigger frequency is higher, it causes a delay of several frames in the acquisition, thus destroying the condition of synchrony between EOL and WFS.
The measurement technique just described doesn't allow to know if the first recorded data refers to the EOL ON or OFF phase; for this reason the two phases will be indicated as A and B for the rest of the discussion. This is not a significant problem because what matters is the wavefront variation and not the absolute value of the Zernike coefficients in the two phases.

The acquired data are subsequently analyzed by a Python program that calculates the difference between the Zernike coefficients of an image taken during phase B and the one taken immediately before, in phase A, this allows to reduce the effects of possible drifts or transients with a characteristic time slower with respect to the sampling rate.

5.1.2 EOL-Pd results

Considering the configuration described in Sec. 4.1, six data acquisitions were taken at different frequencies, in particular the first four samples has a sampling rate, i.e. the trigger frequency, of $4\,Hz$, the fifth one $7\,Hz$ and the last one $4\,Hz$. The reason to take measurements at different frequencies is to verify if the data behavior of the Zernike coefficients in time remains the same. The same trend occurs in all samples. Fig. 5.2 shows the behavior of the Zernike coefficients in time for the first sample. These plots are affected by a big initial transient: this behaviour could be caused by the warming up of the sensor, whose mechanical components have different response times and thermal capacities. Due to this fact the first 10^5 data points are eliminated to perform the analysis.
Fig. 5.3 shows the distribution of the differences between two consecutive images in different phases, i.e. $\Delta c = c^{(A)} - c^{(B)}$, for sample one. Since the data show a normal distribution it is possible to perform a Gaussian fit. The compatibility of the Guassian centroid with zero could mean that the instrument used for these measurements does not have adequate sensitivity.
Since the standard deviation of the mean for each Δc on all the analyzed samples is underestimated, one way to improve the associated error is divide the samples in 150 subgrups for each of which the mean of the Δcs are calculated with the associated error, i.e. the standard deviation. Fig. 5.4 shows the trend of these segmented mean values with respect to the number of the referred segment: note that the various Δc_{sgm}s fluctuate and are also all compatible with zero within the error. Tab. 5.1 shows the various Δcs obtained by taking the average of the segmented subsamples with their standard

deviations. It is evident from the table that, apart from the first sample, the $\Delta c_5 \sim 0$ inside the error. However, the value of the first $\Delta c_5 \sim 10^2\, pm$ is two orders of magnitude larger than theoretical expectations $\Delta c_5^{(Pd)} \simeq 1\, pm$ (see 4.3.2, suggesting some issue with this specific measurement.

$[nm]$	Sample 1	Sample 2	Sample 3	Sample 4	Sample 5	Sample 6
Δc_1	-2.8 ± 0.6	0.3 ± 0.1	-0.4 ± 0.1	-0.3 ± 0.1	-0.2 ± 0.2	0.1 ± 0.3
Δc_2	2.5 ± 0.5	-0.25 ± 0.06	0.24 ± 0.05	0.20 ± 0.09	0.1 ± 0.2	0.0 ± 0.2
Δc_3	0.7 ± 0.3	-0.05 ± 0.06	0.04 ± 0.09	0.04 ± 0.06	0.03 ± 0.08	0.0 ± 0.1
Δc_4	-0.2 ± 0.2	-0.03 ± 0.04	0.02 ± 0.04	0.02 ± 0.05	0.00 ± 0.05	0.00 ± 0.04
Δc_5	-0.3 ± 0.2	0.00 ± 0.04	0.03 ± 0.03	0.00 ± 0.03	0.00 ± 0.03	0.00 ± 0.03
Δc_6	0.2 ± 0.2	-0.01 ± 0.05	0.04 ± 0.04	0.02 ± 0.05	0.00 ± 0.05	-0.01 ± 0.04
Δc_7	0.0 ± 0.1	0.02 ± 0.04	0.00 ± 0.03	0.00 ± 0.05	0.00 ± 0.04	0.00 ± 0.03
Δc_8	-0.4 ± 0.2	0.01 ± 0.03	-0.02 ± 0.03	-0.01 ± 0.02	0.00 ± 0.03	0.00 ± 0.03
Δc_9	-0.10 ± 0.09	0.01 ± 0.02	0.00 ± 0.02	0.00 ± 0.02	0.00 ± 0.03	0.00 ± 0.04
Δc_{10}	2.0 ± 0.2	0.38 ± 0.02	0.37 ± 0.01	0.31 ± 0.02	0.30 ± 0.01	0.36 ± 0.01

Table 5.1: Results of the difference between the Zernike coefficients in the two phases of EOLPd, dividing the sample into subsamples and averaging the obtained values.

Because a few times the sensor misses one or more trigger events, together with the various Zernike coefficients, the Labview program prints also the time elapsed between one measurement and the next one and subsequently the Python program reject those measurements that occurred at an even multiple of the sampling frequency: in this case the SH skips the phase A and immediately jumps to phase B, therefore it is no longer possible to analyze the pair of measurements. Moreover, in this data cleansing procedure, a margin of 125 ms, i.e. the program execution time, it is considered.
Another test performed is to verify that there are no consecutive events with the same values of the Zernike coefficients. This would indicate a buffer refresh problem. There are no events of this type in all the samples analyzed.
All the data acquisitions have been taken during the night to avoid noises of any kind related to the activity of the personell present in the laboratory or temperature drifts related to the air conditioning system.

5.1.3 EOL-Fl results

The same type of analysis is performed for the second EOL with the optical table configuration described in 4.1.1.
As previously said, due to Pockel effect, the higher the voltage applied to the lithium niobate crystal the bigger the alteration of the refractive indices (see Eq. 3.24). To observe this behavior several data acquisitions at different EOL power supply potentials were taken. Even if these samples are also affected by the initial thermal gradient (Fig. 5.5), due to the reduced number of measurements of the sample it is not possible to eliminate the first values to celan up the trend. However this effect is negligible since it has a much greater characteristic time than the sampling time of the WFS $\tau_{thermal} \sim min \gg \tau_{sampling} = 250\, ms$. In Tab. 5.2 are reported the Δcs obtained by averaging the segmented values with their standard deviations, this time segmenting the sample in 50 subsamples. The only value of Δc_5 not compatible with zero is the one for 350 V of power supply. However, it is one order of magnitude lower than theoretical expectations $\Delta c_5^{(Fl)} \simeq nm$ (see 4.3.2) and the incompatibility between the experimental and the theoretical value does not allow to give reliability to the value found experimentally.

Since the WFS calculates the Zernike functions only inside the area defined by the pupil diameter, the choice of the camera aperture size, i.e. the number of lenses of the selected sensor area, influences the reconstruction of the wavefront and his fitting function. To investigate if this dependence significantly affects the Zernike coefficients measurements, various samples with different camera size were taken. These data acquisitions are carried out with an applied potential of 350 V. Because in this case the

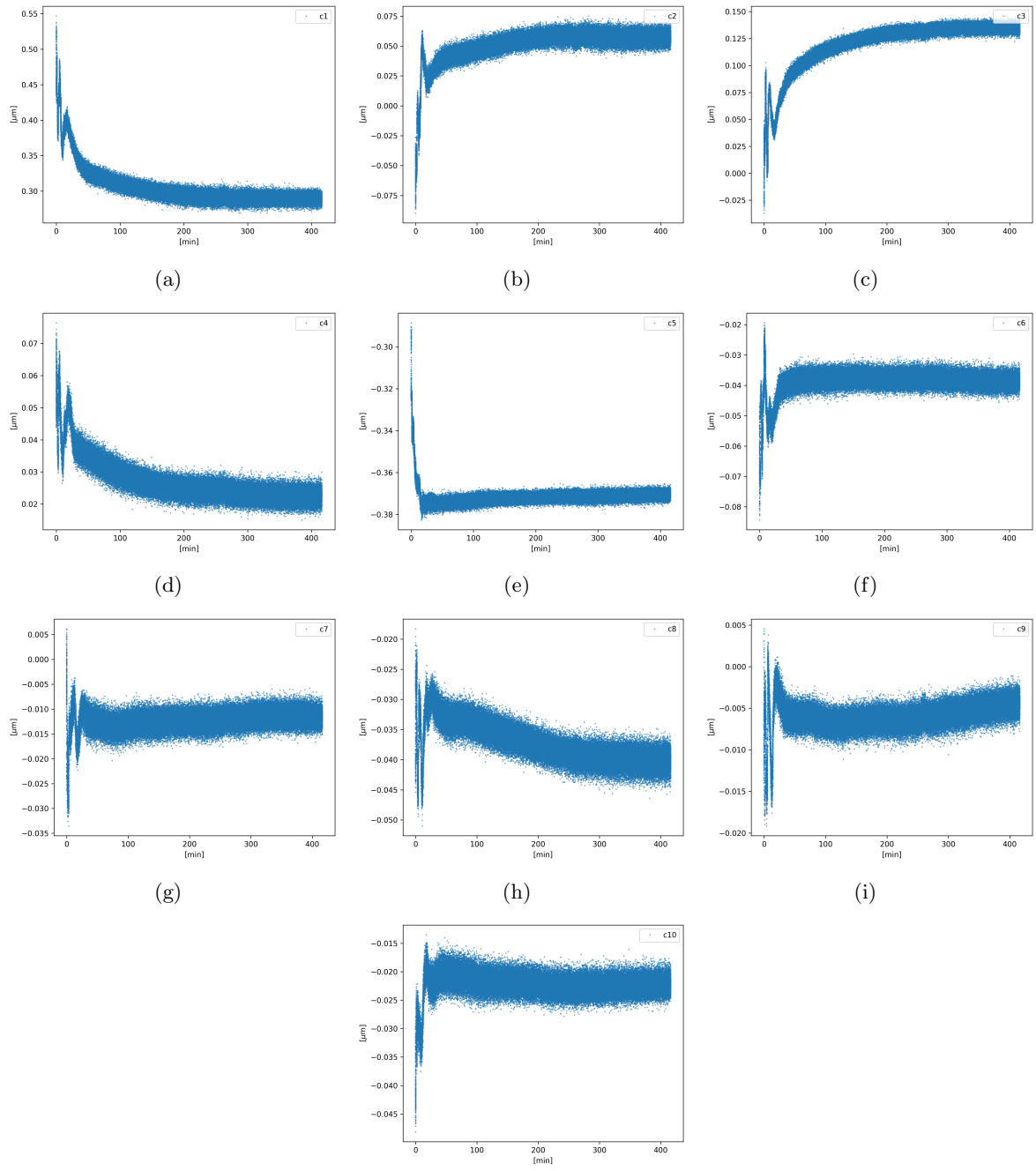

Figure 5.2: Behavior in time of the Zernike coefficients belonging to sample 1.

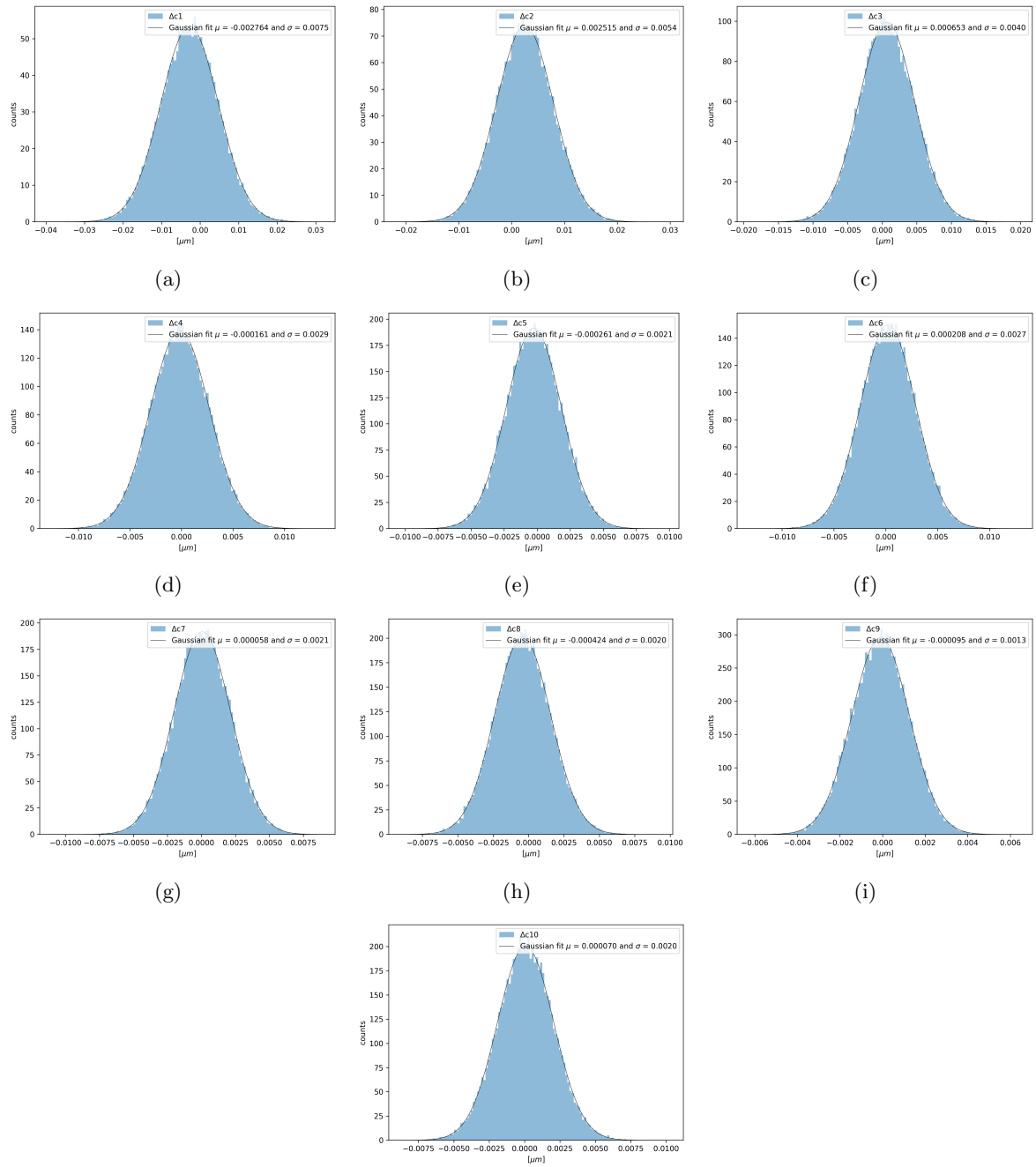

(a) (b) (c)

(d) (e) (f)

(g) (h) (i)

(j)

Figure 5.3: Histogram of the differences of the Zernike coefficients between the two EOL phases, for sample 1.

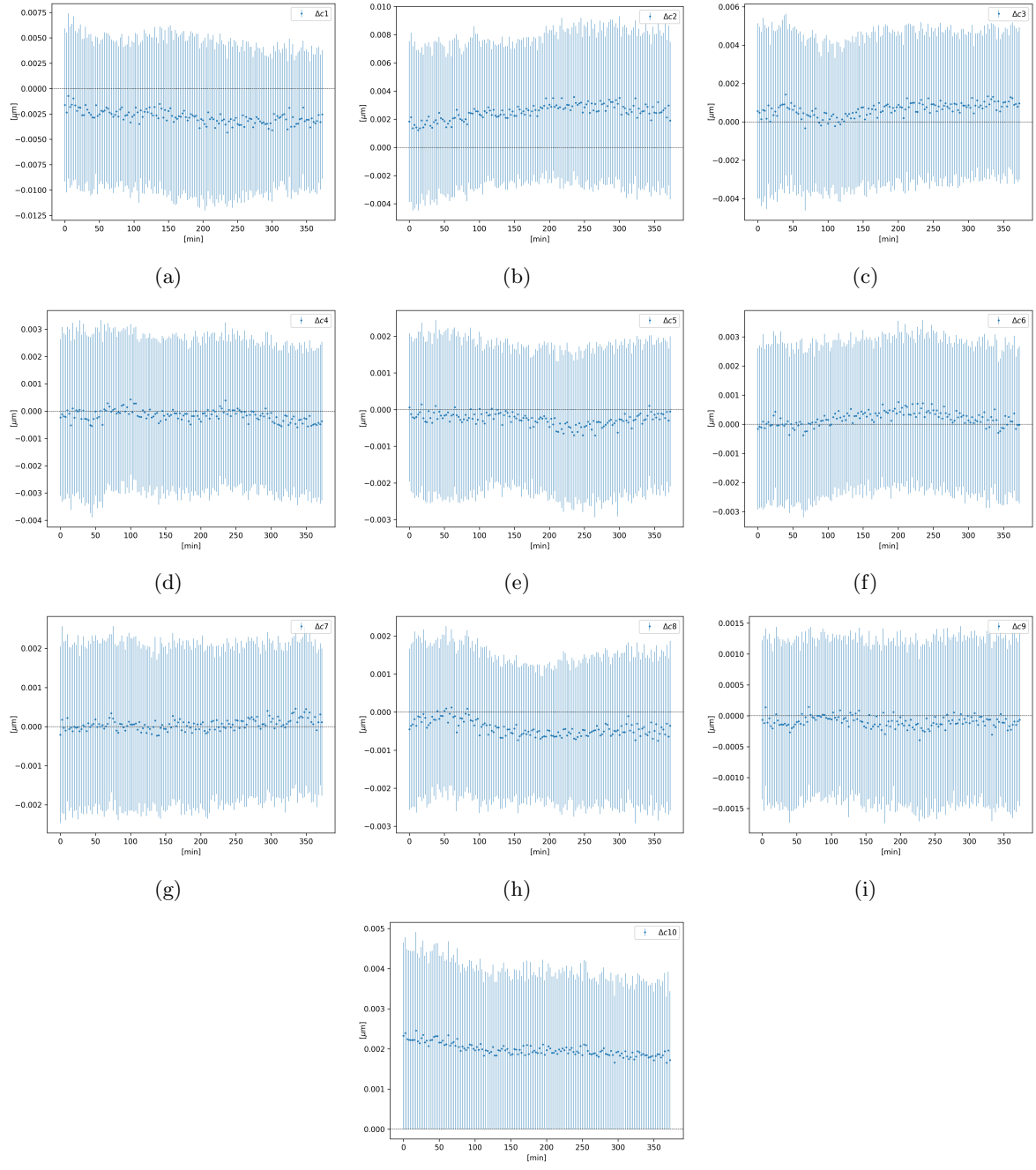

(a) (b) (c)

(d) (e) (f)

(g) (h) (i)

(j)

Figure 5.4: Behavior in time of the Zernike coefficient differences between the two EOL phases obtained averaging the values in each subsample, for sample 1.

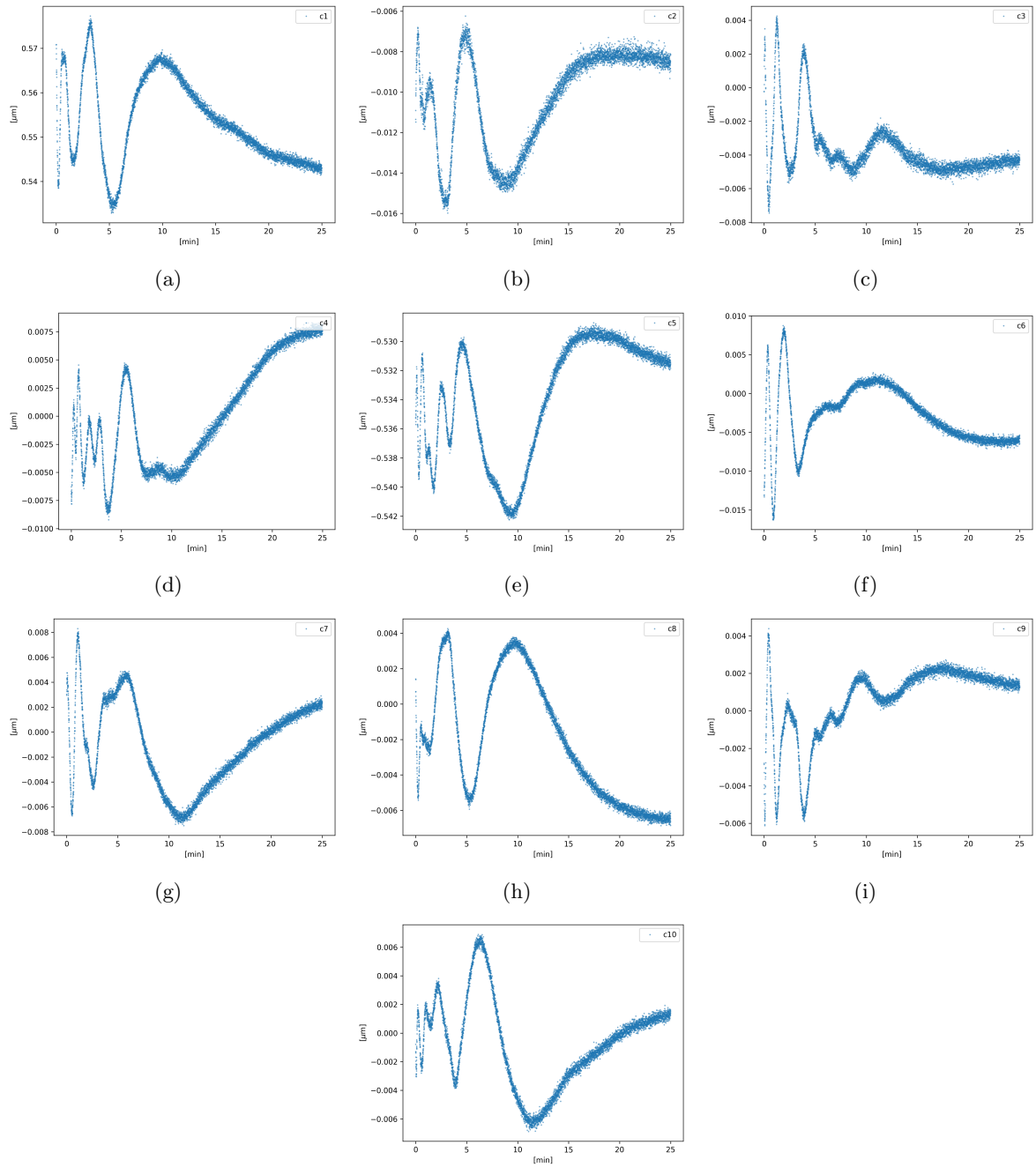

Figure 5.5: Behavior in time of the Zernike coefficients belonging to the sample with the maximum voltage applied.

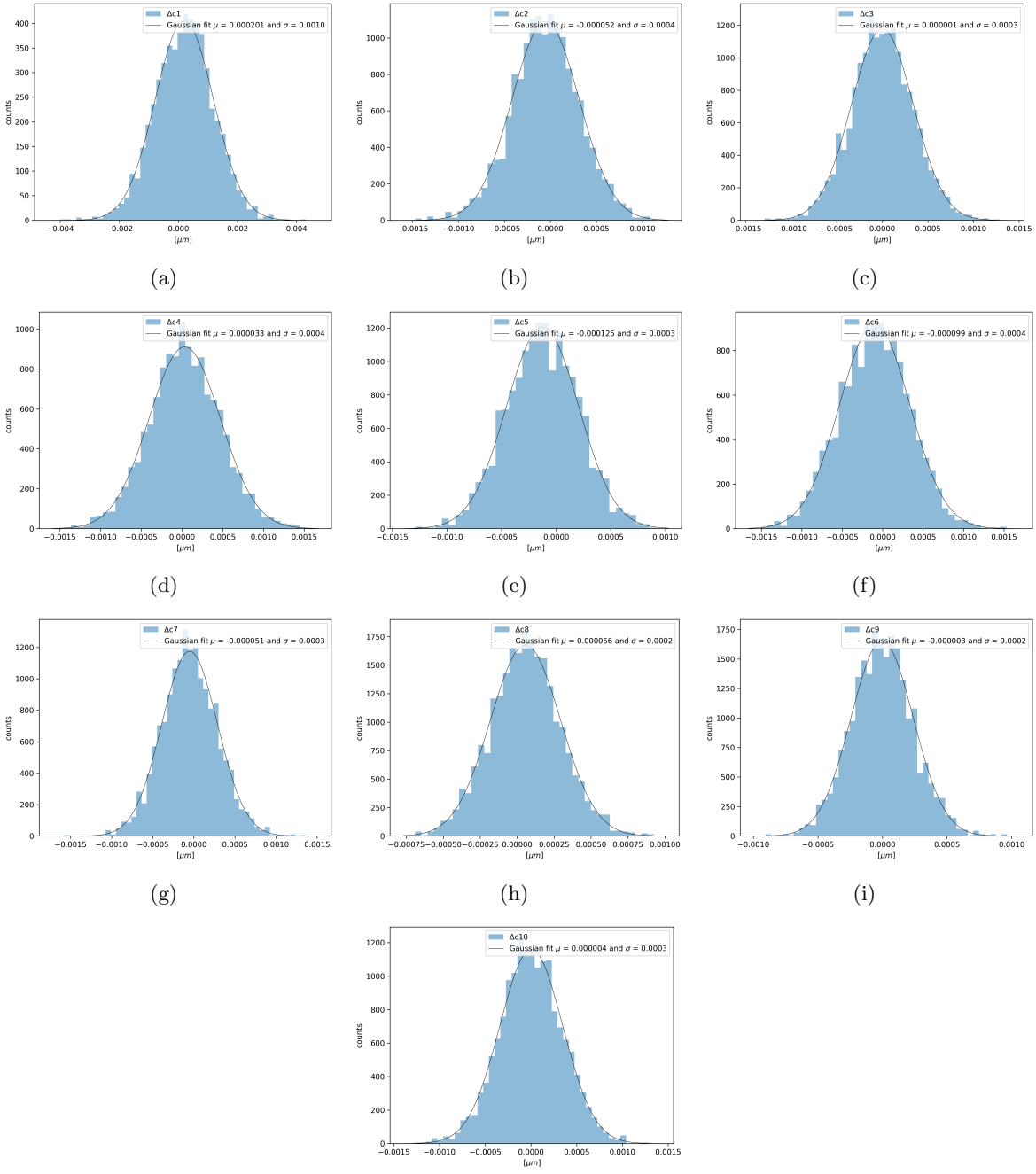

(a) (b) (c)

(d) (e) (f)

(g) (h) (i)

(j)

Figure 5.6: Histogram of the differences of the Zernike coefficients between the two EOL phases, for the sample with the maximum voltage applied.

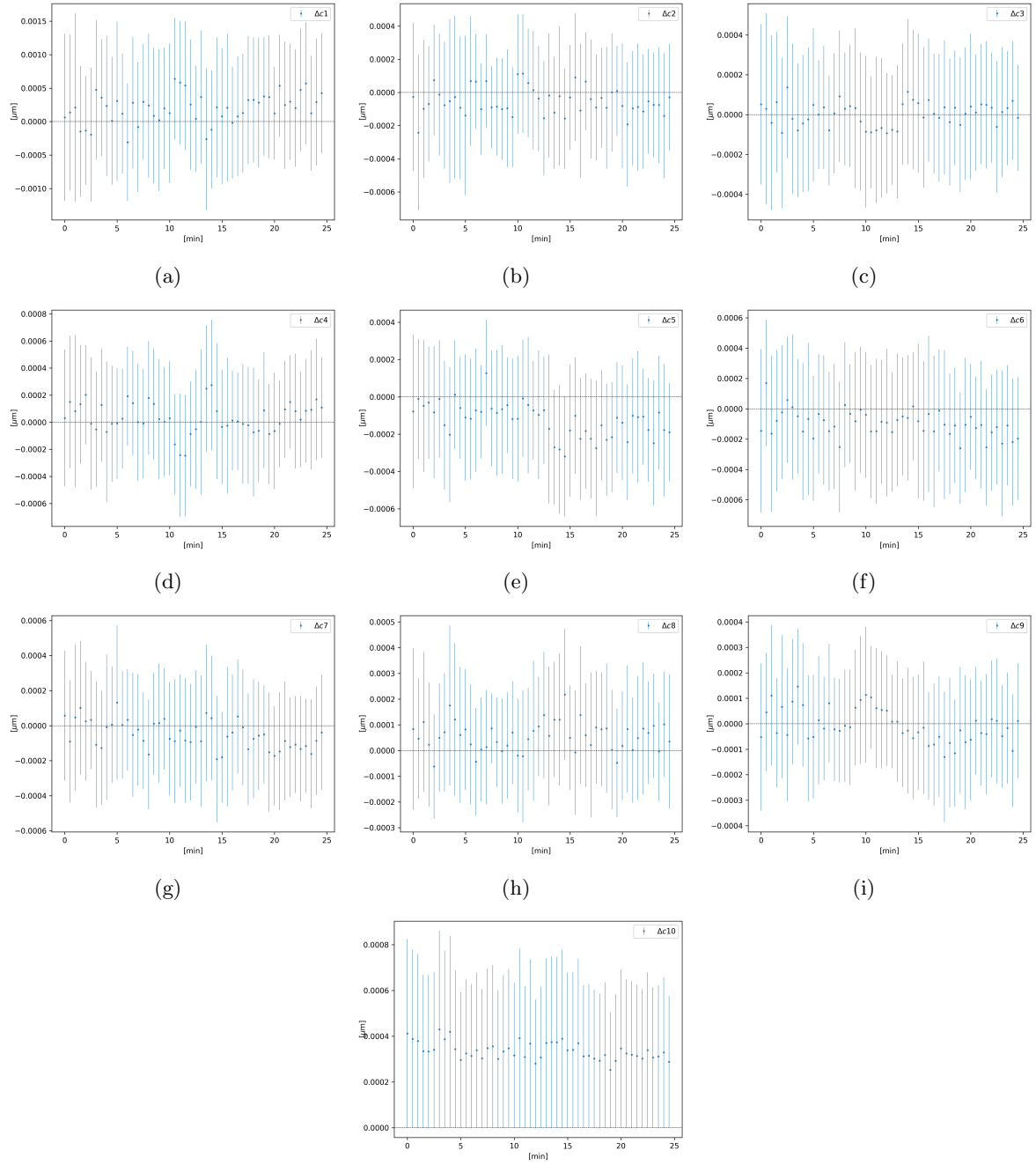

Figure 5.7: Behavior in time of the Zernike coefficient differences between the two EOL phases obtained averaging the values in each subsample, for the sample with the maximum voltage applied.

$[nm]$	$100\,V$	$200\,V$	$300\,V$	$350\,V$
Δc_1	0.0 ± 0.1	0.0 ± 0.2	0.0 ± 0.1	0.2 ± 0.2
Δc_2	-0.01 ± 0.05	0.10 ± 0.09	0.15 ± 0.05	-0.05 ± 0.08
Δc_3	0.00 ± 0.05	0.02 ± 0.08	0.05 ± 0.05	0.00 ± 0.06
Δc_4	0.00 ± 0.07	0.02 ± 0.08	0.03 ± 0.06	0.0 ± 0.1
Δc_5	-0.03 ± 0.05	0.06 ± 0.06	0.06 ± 0.05	-0.12 ± 0.09
Δc_6	-0.01 ± 0.05	-0.04 ± 0.07	-0.11 ± 0.06	-0.10 ± 0.9
Δc_7	0.00 ± 0.04	0.00 ± 0.04	-0.02 ± 0.05	-0.05 ± 0.08
Δc_8	0.01 ± 0.04	-0.03 ± 0.05	-0.07 ± 0.03	0.06 ± 0.06
Δc_9	0.00 ± 0.04	-0.01 ± 0.04	-0.04 ± 0.03	0.00 ± 0.06
Δc_{10}	0.33 ± 0.04	0.31 ± 0.04	0.30 ± 0.03	0.34 ± 0.04

Table 5.2: Results of the difference between the Zernike coefficients in the two phases of EOLFl for different voltages applied, dividing the sample into subsamples and averaging the obtained values.

samples are bigger with respect to the previous ones, to clean up the sample, the first 10^5 measurements were deleted, as in the case described in Sec. 5.1.2, and after that segmented in 150 subsamples. Tab. 5.3 shows all the Δcs obtained by averaging the segmented values with their standard deviations. In particular all the Δc_5 are compatible with zero inside their errors.

$[nm]$	$512\,px$	$768\,px$	$1024\,px$
Δc_1	0.0 ± 0.1	0.0 ± 0.02	0.1 ± 0.1
Δc_2	-0.08 ± 0.08	0.08 ± 0.10	-0.09 ± 0.06
Δc_3	0.02 ± 0.04	0.00 ± 0.03	-0.02 ± 0.03
Δc_4	0.09 ± 0.04	-0.08 ± 0.04	0.00 ± 0.03
Δc_5	-0.03 ± 0.05	0.05 ± 0.04	-0.02 ± 0.03
Δc_6	-0.02 ± 0.07	0.00 ± 0.08	0.02 ± 0.04
Δc_7	0.01 ± 0.05	-0.03 ± 0.03	0.00 ± 0.03
Δc_8	0.04 ± 0.04	-0.04 ± 0.04	0.06 ± 0.03
Δc_9	0.00 ± 0.03	0.00 ± 0.03	0.01 ± 0.02
Δc_{10}	0.37 ± 0.02	0.38 ± 0.02	0.42 ± 0.02

Table 5.3: Results of the difference between the Zernike coefficients in the two phases of EOLFl for different camera size, dividing the sample into subsamples and averaging the obtained values.

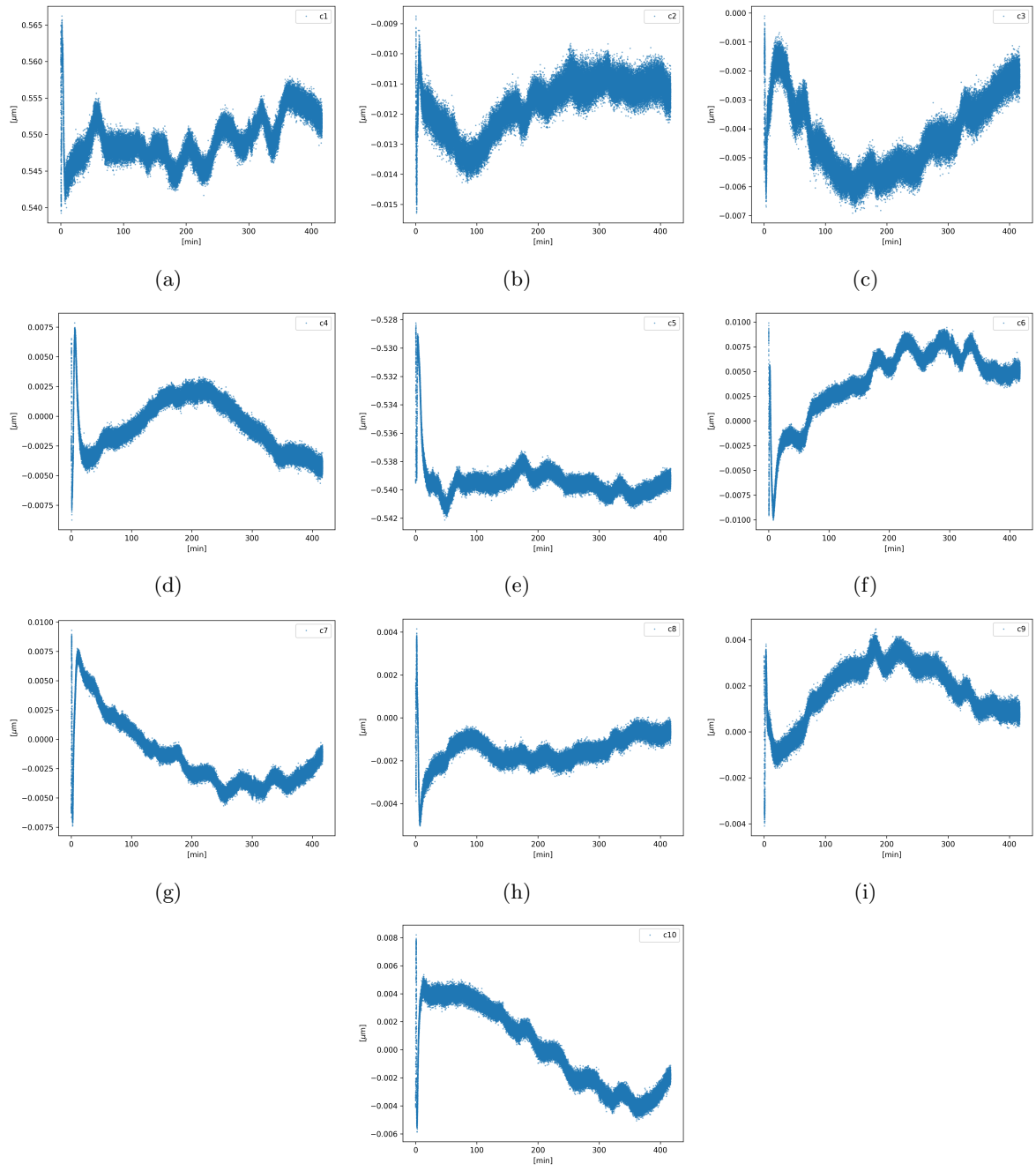

(a) (b) (c)

(d) (e) (f)

(g) (h) (i)

(j)

Figure 5.8: Behavior in time of the Zernike coefficients belonging to the sample with 512 px aperture.

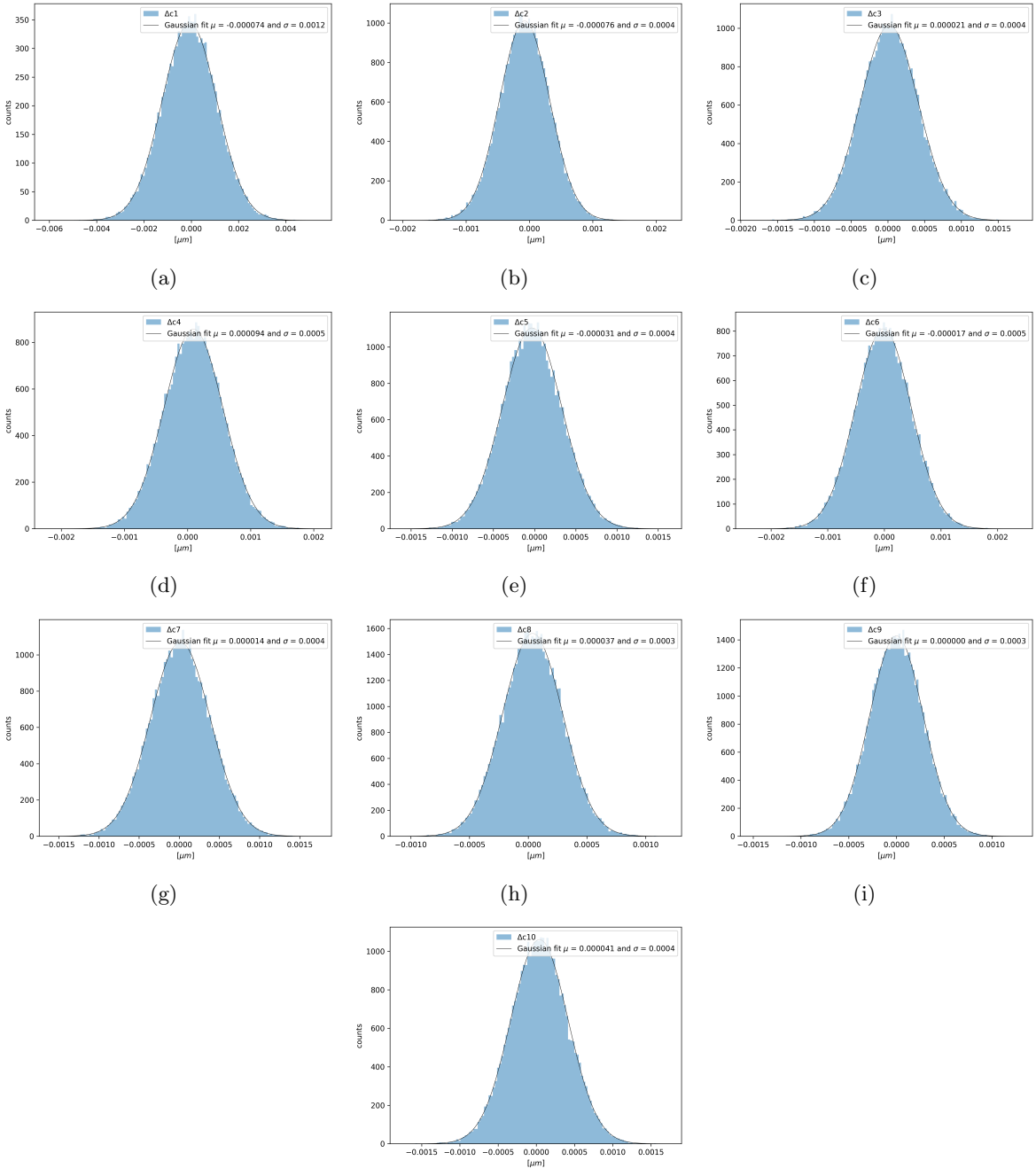

Figure 5.9: Histogram of the differences of the Zernike coefficients between the two EOL phases, for the sample with 512 px aperture.

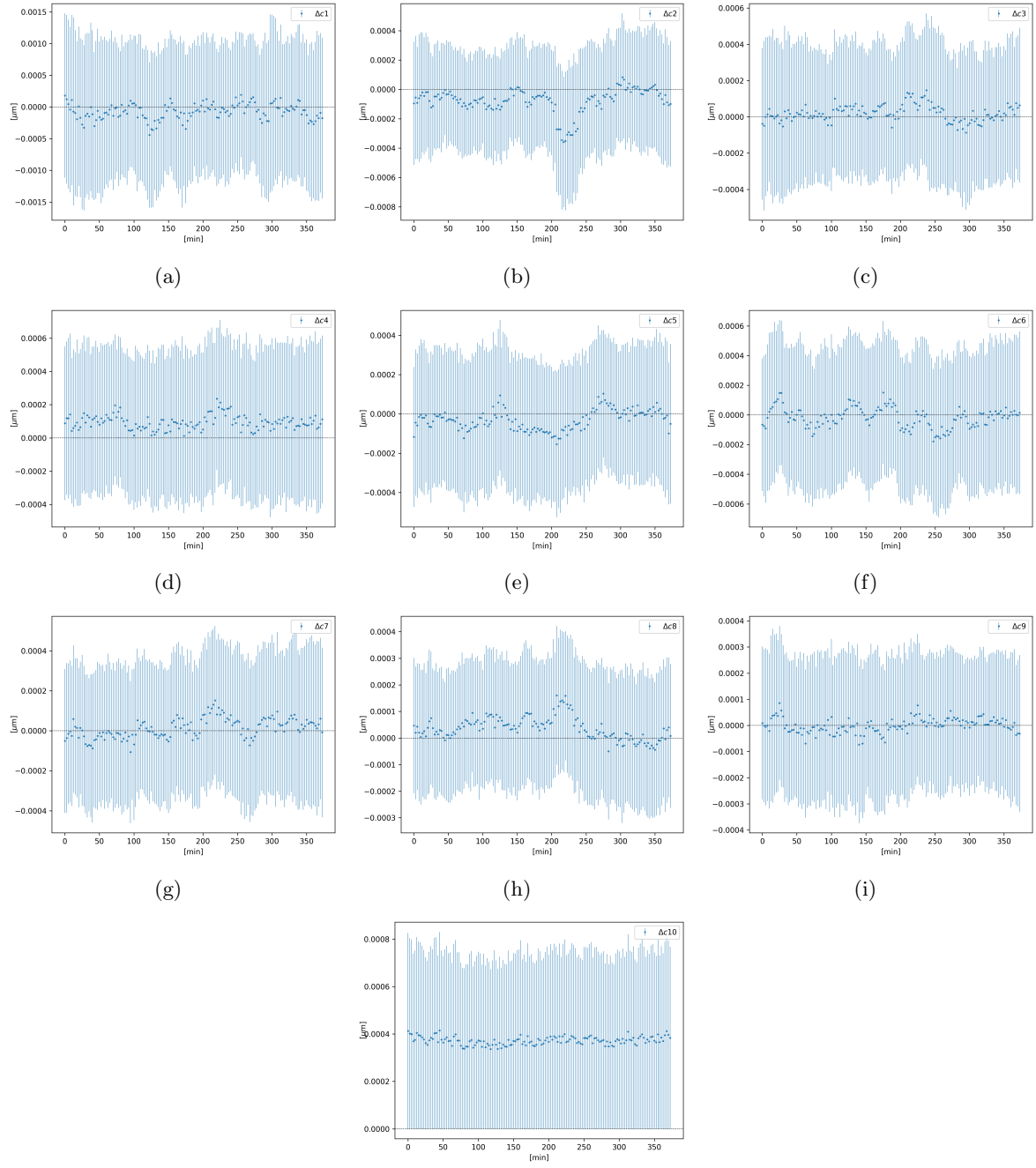

(a) (b) (c)

(d) (e) (f)

(g) (h) (i)

(j)

Figure 5.10: Behavior in time of the Zernike coefficient differences between the two EOL phases obtained averaging the values in each subsample, for the sample with 512 px aperture.

5.1.4 Flip mirror tests

As a check of the instrument and of the analysis procedure I carried out a further study leaving the EOL-Fl OFF and alternately inserting and removing a lens with a focal length $f_{flip} = 1000\,mm$ at $z_{flip} = 38\,cm$. This is expected to provide a signal large enough to be measured, even with the reduced number of samples over which to average due to the fact that the switching is perfomed manually. Fig. 5.11 shows the trend for the single values of the two different phases, with and without the lens. The oscillatory behavior is probably due to the thermal response of the WFS, as previously said.
Due to the reduced number of measurements it is not possible to eliminate the initial thermal transient or to segment the sample into subgroups. By averaging the differences of the subsequent Zernike coefficients one obtains the following results

$$\Delta c_1 = -2 \pm 1\,nm \tag{5.1}$$
$$\Delta c_2 = 0.4 \pm 0.5\,nm \tag{5.2}$$
$$\Delta c_3 = 0.4 \pm 0.4\,nm$$
$$\Delta c_4 = -0.6 \pm 0.7\,nm$$
$$\Delta c_5 = 3.1 \pm 0.5\,nm$$
$$\Delta c_6 = -0.7 \pm 0.7\,nm$$
$$\Delta c_7 = 1.1 \pm 0.3\,nm$$
$$\Delta c_8 = 0.0 \pm 0.3\,nm$$
$$\Delta c_9 = -0.4 \pm 0.4\,nm$$
$$\Delta c_{10} = -0.3 \pm 0.4\,nm$$

The theoretical expectation of the fifth Zernike coefficient and the its difference with and without f_{flip} are

$$c_5^{theo} \simeq -0.5\,\mu m \qquad \Delta c_5^{theo} \simeq 10\,nm. \tag{5.3}$$

The experimental results can be considered reliable considering: the uncertainties in the modeling of the optical system; the fact that the measurement is done manually; the fact that the transient could not be eliminated. A factor of 3 from the expected result proves that the sensor and the analysis procedure work.

For completeness in figure 5.12 the reconstructed wavefront using the Zernike polynomials decomposition using as Zernike coefficients the difference between the averages with and without the lens. I expect to see a pure paraboloid if the only $\Delta c \neq 0$ is the fifth one, i.e. the defocus, but in practice this is not the case since the experimental methodology adopted, that is to manually insert and remove a lens with a flip mount, is highly subject to centering errors. In particular note in 5.1 that also $\Delta c_7 \neq 0$, i.e. the coefficient related to the vertical coma.

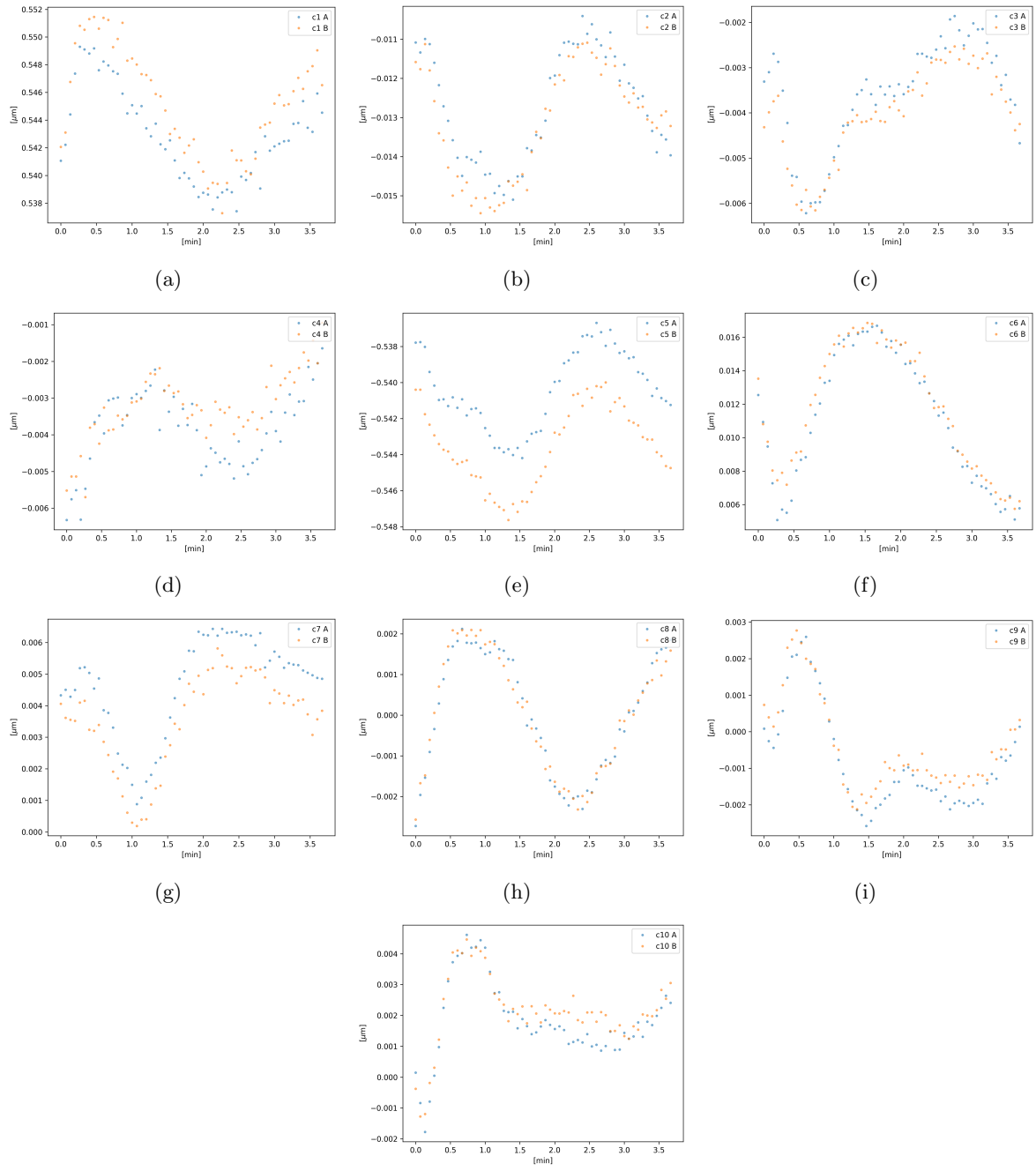

(a) (b) (c)

(d) (e) (f)

(g) (h) (i)

(j)

Figure 5.11: Behavior in time of the Zernike coefficients whose phases indicate if the lens is in between or not.

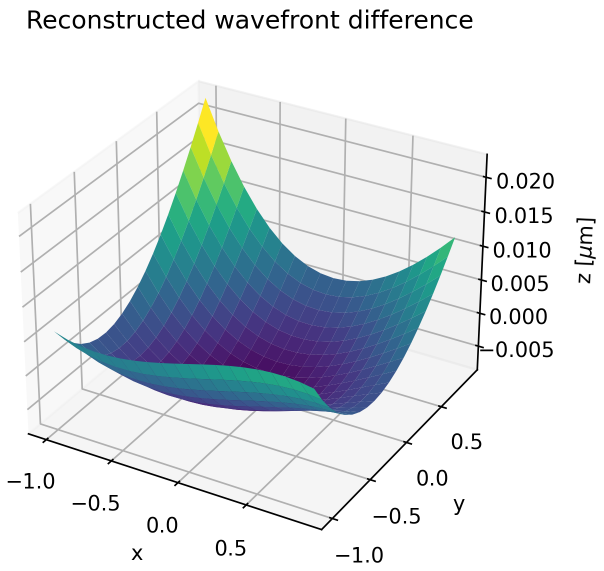

Figure 5.12: Reconstructed wavefront difference with and without f_{flip} using Zernike decomposition.

5.2 Cavity measurements

5.2.1 Methodology

As previously seen in section 4.2, the triangular optical cavity can be used as a mode analyzer by watching the power transmitted by the cavity through a photodiode. By scanning the optical cavity at varying frequencies of the laser light, a forest of peaks is obtained and, once cleaned by a correct alignment, in the spectrum the peaks relative to the 00 mode and those of higher order, i.e. LG10 and HG20-02, are the more evident ones. Since it is expected that the variations induced by the electro-optical modulation of the two EOLs are small and that the fluctuations of the higher order peak heights are not negligible due to vibrations and other environmental factors, one proceeds as in the case of the measurements with the WFS (see Sec. 5.1) by turning the EOL ON and OFF. The power supply for the EOL consists in a square wave. At this point a dedicated Python script identifies the positions of the higher order mode peaks by imposing a low and a high threashold. The program separates the peaks acquired with EOL ON (upper step of the square wave) from those acquired with EOL OFF (lower step).The program then calculates the standard deviation and the average of the grouped data and displays these on a graph.

5.2.2 Results

First of all M_7 is reintroduced on the optical bench, escluding in this way the telescope f_{10} and f_{11} used for the optimization of the beam width for the Shack-Hartmann's analysis (Fig. 4.2). At this point it is possible to measure the effect on the LG10 peak in the case of different voltage applied to the EOL-Fl power supply, in particular a square wave with amplitude $V^{(1)} = 250\,V$ and $V^{(2)} = 400\,V$ with frequency $250\,mHz$ and total acquisition time of $30\,s$.
Fig. 5.13(a) and 5.14(a) shows a difference in the LG10 peak between the ON and OFF phase for the voltage $V^{(1)}$ of $\delta V_{Fl}^{(1)} \simeq 0.8\,mV$. Fig. 5.13(b) and 5.14(b) shows a difference in the LG10 peak between the ON and OFF phase for the voltage $V^{(2)}$ of $\delta V_{Fl}^{(2)} \simeq 1.1\,mV$. The difference in mismatch between the case with EOL-Fl ON and OFF grows as the applied voltage increases.

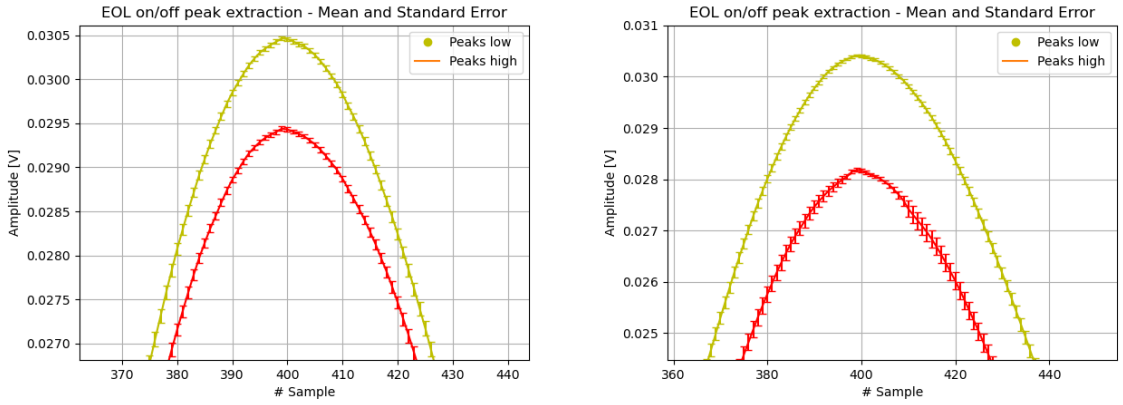

(a) (b)

Figure 5.13: The average height of the peaks obtained with EOL-Fl ON (red line) and EOL-Fl OFF (yellow line). (a) Voltage applied $V^{(1)} = 250\,V$. (b) Voltage applied $V^{(2)} = 400\,V$.

Before this thesis work other cavity measurements were carried out, this time studying the effects of the EOL-Pd. In particular a square wave with amplitude $V^{(2)} = 400\,V$ and frequency $500\,mHz$ is sent to the electro-optical device, recording the transmitted signal for $30\,s$. There is a difference in the height of the LG10 peak between EOL ON and OFF of $\delta V_{Pd} \simeq 1.3\,mV$. Fig. 5.15 shows the difference in the LG10 peak height between the ON and OFF phase of EOL-Pd.

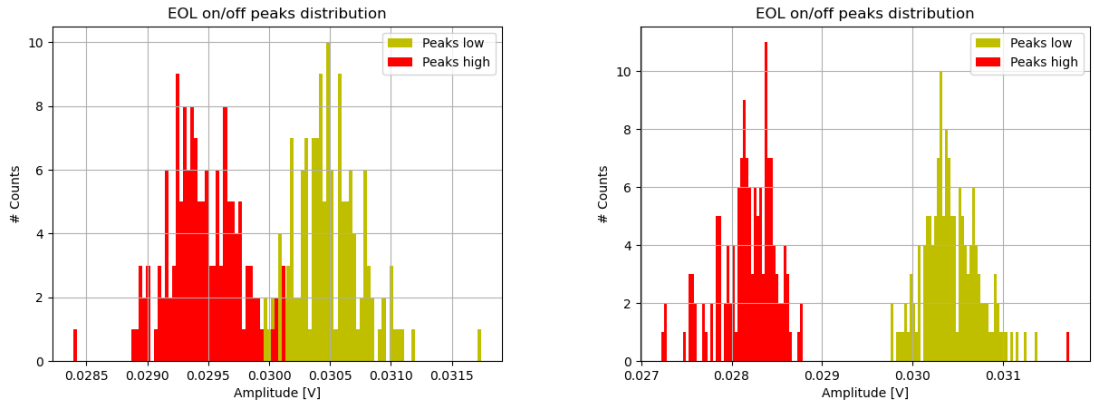

(a) (b)

Figure 5.14: Number of LG10 peaks counted as a function of their voltage amplitude. (a) Voltage applied $V^{(1)} = 250\,V$. (b) Voltage applied $V^{(2)} = 400\,V$.

Comparing the difference in LG10 peak heights for both EOLs at the $V^{(2)} = 400\,V$ power supply potential, notice that they are almost equal $\delta V_{Fl}^{(2)} \simeq \delta V_{Pd} \sim mV$. In both cases this variation in the height of the peak LG10 corresponds to a value of $MM \sim 10\%$. This result is not satisfactory because one would expect an effect for EOL-Fl three order of magnitude bigger than EOL-Pd (see Sec. 4.3.2).

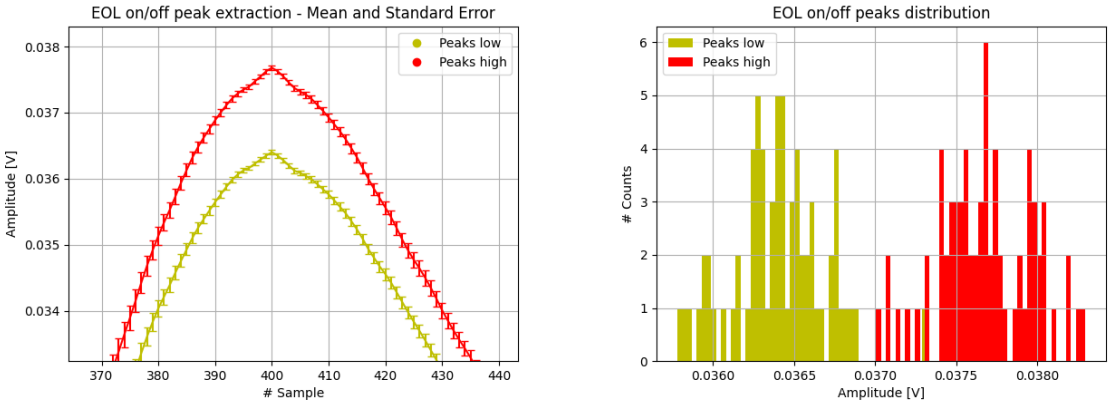

(a) (b)

Figure 5.15: (a) Average height of the peaks obtained with EOL-Pd ON (red line) and EOL-Pd OFF (yellow line). (b) Number of LG10 peaks counted as a function of their voltage amplitude.

Chapter 6

Conclusion

The aim of this thesis was to analyze and study the effects of two different EOL prototype devices on a dedicated bench-top experiment. Two characterization methods are used: the study of wavefront variations using a Shack-Hartmann sensor and the modal analysis inside a triangular optical cavity. Although the cavity measurements previously carried out on EOL-Pd have brought reliable results, the same analysis on the functioning of EOL-Fl was not as satisfactory: in fact, as seen in the Sec. 5.2, by switching ON and OFF both electro-optical devices the same power variation of the higher order modes was found. However, theoretical expectations (see Sec. 4.3.2 and 4.3.2) predict an effect three orders of magnitude higher for EOL-Fl with respect to EOL-Pd. This inconsistency between experimental results and theoretical expectations is not understood and will require further investigation.

Regarding the wavefront variation measurements, both electro-optical devices investigated, have not reached the sensitivity needed to measure their effects. We note however that the choice of the optical telescope to match the beam to the WFS is particularly important: in this thesis it was decided to position the sensor on the plane imaging the output plane of the two electro-optical devices (see Sec. 4.3.2). This choice is justified by the intention to analyze the wavefront shape as it exists for the device. However, in front of the difficulties encountered in reaching the necessary sensitivity, we reconsidered this choice and realized that, as shown in Fig. 6.1, placing the Shack-Hartmann close to the waist position of the resulting beam, the variation of the fifth Zernike coefficient, or Δc_5, can be made substantially larger. By dropping the requirement of working on an image plane, a differently designed optical system could increase the value of Δc_5 by perhaps a few orders of magnitude; this would enable the possibility of measuring it directly with the wavefront sensor which, as seen in the Sec. 4.3, has a sensitivity of around $\lambda/100 \sim 10^{-5}\, mm$.

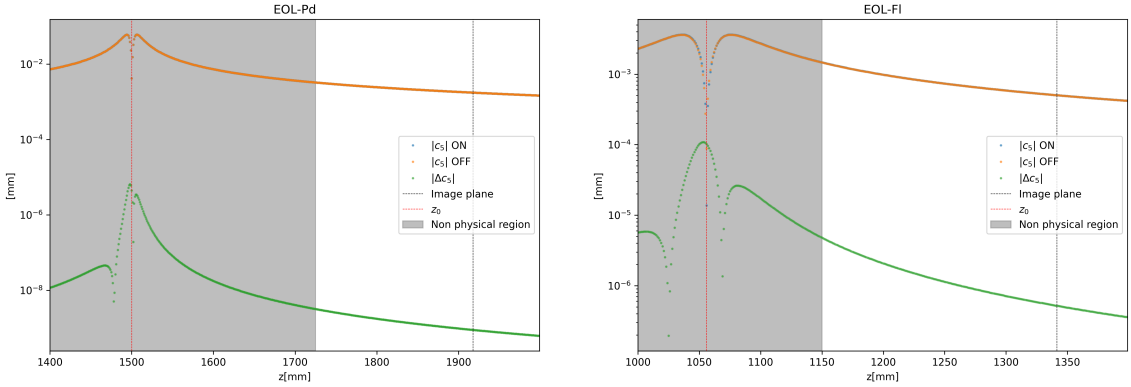

(a) (b)

Figure 6.1: Study of the behavior of Δc_5 by switching ON and OFF EOL-Pd (a) and EOL-Fl (b) as a function of the WFS position. In gray the portion of space occupied by the optics of the matching telescope on the optical bench.

Bibliography

[1] Abbott et al. Observation of gravitational waves from a binary black hole merger. *Physical review letters*, 116(6):061102, 2016.

[2] Abernathy et al. Einstein gravitational wave telescope conceptual design study. 2011.

[3] Araya et al. Optical mode cleaner with suspended mirrors. *Applied optics*, 36(7):1446–1453, 1997.

[4] RW Boyd. Nonlinear optics, academic press, san diego 1992. *P. S. Pershan. Phys. Rev.*, 121:1963.

[5] Warde C. Class notes for modern optics project laboratory - optical signals, devices and systems - geometric optics. 2007.

[6] Matteo Carlassara. A novel technique for laser mode-matching in gravitational wave detectors.

[7] Sean M Carroll. *Spacetime and geometry*. Cambridge University Press, 2019.

[8] Carlton M Caves. Quantum-mechanical radiation-pressure fluctuations in an interferometer. *Physical Review Letters*, 45(2):75, 1980.

[9] Carlton M Caves. Quantum-mechanical noise in an interferometer. *Physical Review D*, 23(8):1693, 1981.

[10] Fulda et al. Alignment sensing for optical cavities using radio-frequency jitter modulation. *Applied Optics*, 56(13):3879–3888, 2017.

[11] Massimo Granata, Christelle Buy, Robert Ward, and Matteo Barsuglia. Higher-order laguerre-gauss mode generation and interferometry for gravitational wave detectors. *Physical review letters*, 105(23):231102, 2010.

[12] Herwig Kogelnik and Tingye Li. Laser beams and resonators. *Applied optics*, 5(10):1550–1567, 1966.

[13] Fabian Magana-Sandoval, Thomas Vo, Daniel Vander-Hyde, JR Sanders, and Stefan W Ballmer. Sensing optical cavity mismatch with a mode-converter and quadrant photodiode. *Physical Review D*, 100(10):102001, 2019.

[14] Michele Maggiore. *Gravitational waves: Volume 1: Theory and experiments*. OUP Oxford, 2007.

[15] Martynov et al. Sensitivity of the advanced ligo detectors at the beginning of gravitational wave astronomy. *Physical Review D*, 93(11):112004, 2016.

[16] Mueller et al. Determination and optimization of mode matching into optical cavities by heterodyne detection. *Optics letters*, 25(4):266–268, 2000.

[17] Nicolò Pisani. Sviluppo di una lente elettro-ottica per misure di accoppiamento laser in cavità a radiofrequenza.

[18] Bahaa EA Saleh and Malvin Carl Teich. *Fundamentals of photonics*. john Wiley & sons, 2019.

[19] Anthony E Siegman. *Lasers*. University science books, 1986.

[20] A. M. Thomas. Mode mismatch detection using an electro-optic lens device. `http://www.phys.ufl.edu/ireu/IREU2019/pdf_reports/Ann_Mariam_Thomas_Report_final_IREU_Padova.pdf`, 2010.

[21] Thorlabs. Optical Wavefront Sensors (Shack-Hartmann) - Operation Manual. `https://www.thorlabs.com/_sd.cfm?fileName=MTN003815-D02.pdf&partNumber=WFS30-5C/M`, 2020.

[22] RS Weis and TK Gaylord. Lithium niobate: Summary of physical properties and crystal structure. *Applied Physics A*, 37(4):191–203, 1985.